LETTER

doi:10.1038/nature19058

A trans-synaptic nanocolumn aligns neurotransmitter release to receptors

Ai-Hui Tang[1,2]*, Haiwen Chen[1,2,3]*, Tuo P. Li[1,2,3], Sarah R. Metzbower[1,2], Harold D. MacGillavry[4] & Thomas A. Blanpied[1,2]

Synaptic transmission is maintained by a delicate, sub-synaptic molecular architecture, and even mild alterations in synapse structure drive functional changes during experience-dependent plasticity and pathological disorders[1,2]. Key to this architecture is how the distribution of presynaptic vesicle fusion sites corresponds to the position of receptors in the postsynaptic density. However, while it has long been recognized that this spatial relationship modulates synaptic strength[3], it has not been precisely described, owing in part to the limited resolution of light microscopy. Using localization microscopy, here we show that key proteins mediating vesicle priming and fusion are mutually co-enriched within nanometre-scale subregions of the presynaptic active zone. Through development of a new method to map vesicle fusion positions within single synapses in cultured rat hippocampal neurons, we find that action-potential-evoked fusion is guided by this protein gradient and occurs preferentially in confined areas with higher local density of Rab3-interacting molecule (RIM) within the active zones. These presynaptic RIM nanoclusters closely align with concentrated postsynaptic receptors and scaffolding proteins[4–6], suggesting the existence of a trans-synaptic molecular 'nanocolumn'. Thus, we propose that the nanoarchitecture of the active zone directs action-potential-evoked vesicle fusion to occur preferentially at sites directly opposing postsynaptic receptor–scaffold ensembles. Remarkably, NMDA receptor activation triggered distinct phases of plasticity in which postsynaptic reorganization was followed by trans-synaptic nanoscale realignment. This architecture suggests a simple organizational principle of central nervous system synapses to maintain and modulate synaptic efficiency.

The location of vesicle fusion within an active zone is probably dictated by a few key members of the presynaptic proteome, including RIM1/2, Munc13, and bassoon (Bsn)[7] (Fig. 1a). To explore the organization of these proteins, we studied their subsynaptic distribution relative to postsynaptic scaffolding protein PSD-95 in cultured hippocampal neurons using 3D-STORM[8] following immunolabelling using primary antibodies and Alexa647- or Cy3-tagged secondary antibodies (Fig. 1b). Paired synaptic clusters of active zone protein and PSD-95 with clear borders were selected. As a confirmation that these pairs constituted synapses, we measured the peak-to-peak distances between pre- and postsynaptic clusters and found them to be consistent with previous measurements[9] (Extended Data Fig. 1).

The distribution of RIM1/2 within the active zone, measured as 3D local density, was distinctively non-uniform with notable high-density peaks, which we characterized as nanoclusters (Fig. 1c, e). We adapted an auto-correlation function (ACF) to test whether this distribution occurs more frequently than expected by chance. The measured ACF showed significant non-uniformity compared to random ensembles (Fig. 1d). Simulations showed that the distance for which the ACF was significantly elevated provided a means to estimate the nanocluster diameter (Extended Data Fig. 2a–c). The average estimated diameter of ~80 nm for RIM1/2 nanoclusters was very close to the reported size of PSD-95 and AMPA receptor (AMPAR) nanoclusters[4–6]. Similar distribution and nanocluster properties were found using a different antibody targeted towards a separate epitope in RIM1 (Extended Data Fig. 2d). Isolated non-synaptic small groups of localizations showed a weaker ACF that was significant over a much smaller distance (Fig. 1d). This and other experiments suggest that the measured non-uniformity was not likely due to over-counting molecules or to potential artefacts of primary–secondary antibody labelling (Extended Data Fig. 3).

To directly compare the nanoscale organization of key active zone proteins, we developed an algorithm that identified nanoclusters based on local densities (Fig. 1e). Nanoclusters of each protein were more likely to be located near the centre of synapses than near the edge (Fig. 1f, Extended Data Fig. 2i). Compared to PSD-95 as the common control in pairwise two-colour experiments, there were similar numbers of RIM1/2, more Munc13, and fewer Bsn nanoclusters per synapse (Fig. 1h). Comparisons between these three proteins suggested that Munc13 had a wider distribution than RIM1/2 across the active zone and the distribution of Bsn was closer to uniform throughout the synapse (Fig. 1g–i, Extended Data Fig. 2f–n). Together, these observations revealed a complex and heterogeneous molecular architecture within single synapses, typified by dense assemblies of fusion-associated proteins nearer the centre.

To examine the potential functional impact of the active zone nanoclusters on vesicle fusion[10,11], we sought to directly map the distribution of vesicle fusion sites over multiple release events within individual boutons. To do so, we adapted analysis for single-molecule localization to signals from single-vesicle fusion obtained with vGlut1–pHluorin–mCherry (vGpH). Neurons were cotransfected with cyan fluorescent protein (CFP)-tagged synapsin1a (Syn1a), a vesicle-associated protein that marks boutons, and vGpH, which increases in green fluorescence intensity upon vesicle fusion[12]. Single electrical field stimuli evoked vesicle fusion (Fig. 2a, b, Extended Data Fig. 4a) with a release probability (P_r) of 0.11 ± 0.01 (mean $\pm$ s.e.m.) per bouton, comparable to previous measurements, which was also sensitive to extracellular Ca^{2+} (Extended Data Fig. 4b–d), as expected. In the presence of TTX, the frequency of action-potential-independent spontaneous release events detected with vGpH was similar to the frequency of NMDA receptor (NMDAR)-dependent postsynaptic Ca^{2+} transients measured separately using the Ca^{2+} sensor GCaMP6f (Extended Data Fig. 5a).

To determine whether these evoked fusion events represent single- or multi-vesicular fusion, we compared them with spontaneous release under TTX conditions (Fig. 2a–c), which most likely arises from single vesicle fusion[13]. By fitting the photon number distributions of evoked and spontaneous events, we estimated that ~72–82% of evoked events arose from single-vesicle fusion (Fig. 2c). With the majority of evoked release stemming from single-vesicle fusion, the location of fusion may be deduced by mathematically fitting the fluorescence profile captured immediately after fusion (Fig. 2d), analogous to single-molecule

[1]Department of Physiology, University of Maryland School of Medicine, Baltimore, Maryland 21201, USA. [2]Program in Neuroscience, University of Maryland School of Medicine, Baltimore, Maryland 21201, USA. [3]Medical Scientist Training Program, University of Maryland School of Medicine, Baltimore, Maryland 21201, USA. [4]Cell Biology, Department of Biology, Faculty of Science, Utrecht University, 3584 CH Utrecht, The Netherlands.
*These authors contributed equally to this work.

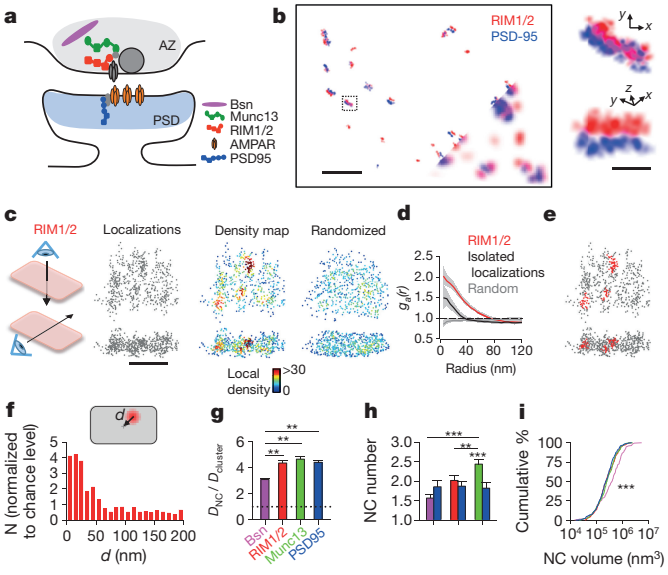

Figure 1 | Vesicle release proteins form subsynaptic nanoclusters. **a**, Colour-coded schematic of studied synaptic proteins. AZ, active zone; PSD, postsynaptic density. **b**, Synapses labelled with RIM1/2 and PSD-95 imaged using 3D-STORM (10-nm pixels) compared to wide-field composite (bottom corner, 100-nm pixels). Scale bar, 2 μm. Boxed synapse enlarged in original (top) and rotated (bottom) angles. Scale bar, 200 nm. **c**, *En face* (top) and side (bottom) views of a RIM1/2 cluster showing all localizations and local density maps for a measured synaptic cluster compared to a simulated randomized cluster. Scale bar, 200 nm. **d**, Auto-correlation functions of measured RIM1/2 ($n = 115$), isolated non-synaptic small groups of localizations due to repetitive switching of fluorophores ($n = 42$), and simulated randomized ($n = 115$) distributions. **e**, RIM1/2 nanoclusters (red) within a synaptic cluster. **f**, Distribution of nanocluster distances from the centre of synapses normalized to randomized distribution. **g**, Molecule density inside nanoclusters (NC) normalized to synaptic average. **h**, Average number of protein nanoclusters per synapse. **i**, Cumulative distributions of nanocluster volumes. $*P < 0.05$; $**P < 0.01$; $***P < 0.001$, one-way ANOVA on ranks with pairwise comparison procedures (Dunn's method) for **g**, **h** and Kolmogorov–Smirnov test for **i**. All experiments were repeated ≥3 times. Also see Extended Data Fig. 3 and Supplementary Table 1.

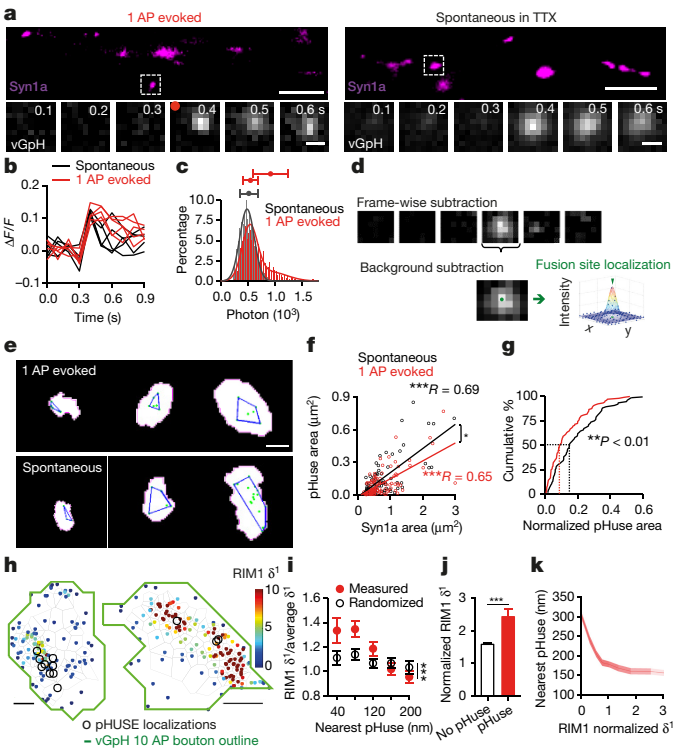

Figure 2 | Release site mapping by pHuse in single synapses shows RIM predicts evoked fusion distribution. **a**, Neurons co-expressing Syn1a–CFP (top; scale bars, 5 μm), identifying synaptic boutons, and vGpH (bottom; scale bars, 500 nm), used to detect vesicle fusion with fluorescence increases from single action potential (AP)-evoked and spontaneous release. **b**, Example of fluorescence traces from evoked and spontaneous events over repeated trials at single boutons. **c**, Photon count distributions for detected spontaneous events fit with a normal distribution ($\mu = 512$, $\sigma = 167$) and evoked events fit with a mixture of two normal distributions ($\mu_1 = 542$, $\sigma_1 = 143$, $\mu_2 = 912$, $\sigma_2 = 319$). Filled circles with error bars show mean ± s.d. of normal curves. **d**, Image processing steps in pHuse to determine fusion site locations. **e**, Fusion sites (green points) and area of fusion (blue line) from boutons of different sizes defined with Syn1a (white). Scale bar, 500 nm. **f**, Correlation between fusion area and bouton size, linear fit. Correlations are significantly different, ANCOVA, $F_{1,171} = 5.01$. **g**, Cumulative distributions of fusion areas normalized to bouton size (Kolmogorov–Smirnov test, $**D = 0.26$). **f**, **g**, $n_{spontaneous} = 77/22$, $n_{evoked} = 104/28$. **h**, Tessellated RIM1-mEos and pHuse localizations over the same boutons. Scale bars, 200 nm. **i**, Tesseler first-rank density (δ^1) for RIM1 measured versus randomized distributions as a function of distance from pHuse localizations. **j**, Comparison within boutons of average δ^1 for RIM1 localizations within 40 nm to a pHuse localization versus not. **k**, Average nearest pHuse distance as a function of RIM1 δ^1. **i**, **j**, $n = 26/13$ $*P < 0.05$, $**P < 0.01$, $***P < 0.001$. *n* given in synapses/experiments. Also see Extended Data Figs 4–6.

localization techniques[14]. For our median count of 518 photons per localization, the effective localization precision was in practice limited by vesicle diameter. In individual boutons, multiple evoked or spontaneous single-vesicle fusion events were used to generate maps that defined the areas over which vesicle fusion occurred (Fig. 2e, Extended Data Fig. 4e–l). We called this approach 'pHluorin uncovering sites of exocytosis' or pHuse.

Fusion site areas for spontaneous and evoked vesicle fusion tightly correlated with bouton areas measured by Syn1a (Fig. 2f), as expected. However, the slopes of the correlations differed, even though the bouton sizes were similar between groups (Extended Data Fig. 5b). In fact, evoked fusion site areas were significantly smaller (median smaller by 48%) and occurred over a significantly smaller proportion of the bouton (median smaller by 39%) than spontaneous fusion (Fig. 2g, Extended Data Fig. 5c, d, h–j).

One interpretation is that the concentration of vesicle priming proteins in nanoclusters favours evoked fusion in these subregions of the active zone. This predicts that pHuse events would be associated with higher local RIM1 density and conversely that high local density of RIM1 increases the probability of nearby fusion. To assess these predictions, we mapped vesicle fusion sites relative to Eos3-tagged RIM1 using sequential PALM-pHuse imaging on the same live boutons (Fig. 2h, Extended Data Fig. 6d, e). As a local density metric for RIM1, we applied Voronoi tessellation and measured the first-rank density (δ^1) for each RIM1–mEos3 localization (as described in ref. 15).

The distribution of RIM1–mEos3 was non-uniform and contained nanoclusters with an average diameter of 80.95 ± 5.34 nm and 78.93 ± 5.85 nm using either an adapted SR-Tesseler analysis[15] or nearest neighbour distance analysis[4], respectively (Extended Data Fig. 6f), consistent with our 3D-STORM results (Fig. 1). We then compared δ^1 as a function of distance from the nearest pHuse localization for the measured RIM1 distributions versus randomized RIM1 distributions generated from the same number of localizations over the same area. Indeed, near pHuse sites, the average RIM1 δ^1 was significantly greater than chance (Fig. 2i). Furthermore, within individual boutons, RIM1 molecules within 40 nm of a pHuse location had significantly higher δ^1 than those further away (Fig. 2j). Conversely, considering all individual RIM1 localizations, the distance from the nearest pHuse localization decreased as a function of RIM1 δ^1 (Fig. 2k).

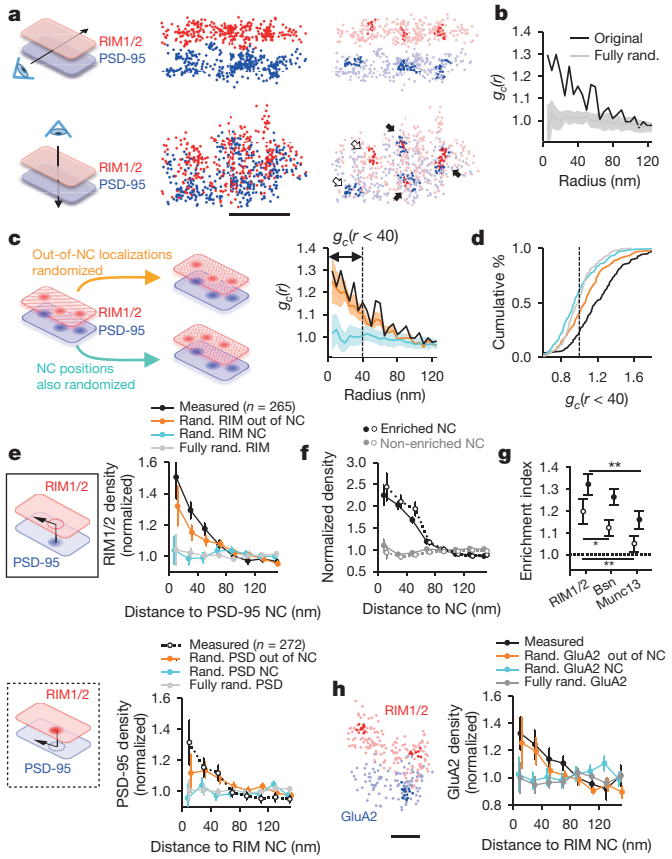

Figure 3 | Trans-synaptic nanoscale alignment of active zone and PSD proteins. a, Distributions of synaptic RIM1/2 and PSD-95 pair as the original localizations (left) and with nanoclusters highlighted (right). Scale bar, 200 nm. Filled arrows indicate aligned nanoclusters, open arrows denote non-aligned nanoclusters. **b**, Paired correlation function (PCF) of measured RIM1/2 and PSD-95 compared to PCF with either distribution randomized. **c**, PCF of simulated distributions with (cyan) and without (orange) shuffling nanocluster positions. **d**, Cumulative distributions of cross-correlation index ($n = 143$ synapses). **e**, RIM1/2 protein enrichment as a function of distance from translated PSD-95 nanocluster centres (top, filled points) and PSD-95 enrichment relative to RIM1/2 nanoclusters (bottom, open points). Simulations with same randomizations as in **d**, **e** were performed for each synapse. **f**, Protein density profile for enriched versus non-enriched nanoclusters, $n = 119$ PSD-95 nanoclusters, 90 RIM1/2 nanoclusters. **g**, Enrichment indices for RIM1/2, Munc13, and Bsn relative to PSD-95 nanoclusters (filled) and for the opposite direction (open), $n > 260$ nanoclusters, $^*P < 0.05$; $^{**}P < 0.01$, ANOVA on ranks with Dunn's method. **h**, GluA2 enrichment with respect to RIM1/2 nanoclusters, $n = 36$ synapses. Scale bar, 100 nm. All experiments were repeated ≥3 times. Also see Extended Data Fig. 6 and Supplementary Table 2.

Thus, nanodistribution of RIM predicts the local probability of evoked fusion.

For the synapse as a whole, the impact of presynaptic nanoscale organization and confined vesicle sites (Figs 1 and 2) will depend strongly on whether these RIM nanoclusters align with postsynaptic receptor nanoclusters[4]. To assess this, we compared the distribution of PSD-95 over the face of individual synapses to the corresponding distributions of RIM1/2, as the PSD-95 nanoclusters concentrate higher density of receptors[7]. An example synapse, presented in Fig. 3a (Supplementary Video 1), shows three RIM1/2 nanoclusters and three PSD-95 nanoclusters that appear well-aligned and one pair not aligned. We used two independent approaches to assess the relationship between active zone and postsynaptic density (PSD) protein distributions. First we adapted a paired cross-correlation function (PCF) to measure the spatial relationship between the two distributions (see Methods). The measured active zone–PSD distributions showed a significantly elevated PCF compared to simulated active zone–PSD distributions with either distribution fully randomized (Fig. 3b). We then tested the contribution of nanocluster positions to this elevated PCF (Fig. 3c). Randomizing nanocluster positions and out-of-nanocluster molecules (keeping localizations within nanocluster borders intact) abolished the PCF to chance level, while randomizing just the out-of-nanocluster molecules only modestly reduced the PCF, indicating that the precise positioning of the nanoclusters themselves dominate the overall correlation of protein distributions (Fig. 3c, d).

Second, we reasoned that if synapses were trans-synaptically aligned on the nanoscale level, the protein distribution on one side of the synapse would predict protein density in the opposing neuron. To test this, we measured RIM1/2 localization densities as a function of radial distance from the centres of PSD-95 nanoclusters as translated across the synaptic cleft (Fig. 3e). RIM1/2 localization densities within a 60 nm radius were significantly higher than the synaptic cluster average, decaying e-fold per 43.2 ± 12.1 nm away from the peak. This enrichment was again principally dependent on the relative positioning of nanoclusters within synaptic clusters (Fig. 3e). For each individual nanocluster, we defined an enrichment index as the average molecular density of the opposed protein within a 60 nm radius from the nanocluster centre (Extended Data Fig. 7a). Nanoclusters with enrichment indices significantly greater than that of the fully randomized distribution were considered enriched (Fig. 3f). We found 44.4 ± 3.0% of PSD-95 nanoclusters to be enriched (Extended Data Fig. 7b), and these nanoclusters were opposed to RIM1/2 molecule densities that were 2.0 ± 0.1 times the average RIM1/2 synaptic cluster density (Fig. 3f). A similar PSD-95 protein enrichment profile was found relative to the centres of RIM1/2 nanoclusters (Fig. 3e). Thus, this detailed metric for assessing nanoscale alignment revealed strong co-enrichment of these key proteins along narrow, transcellular columns. In comparison to RIM1/2, the enrichment of Munc13 with respect to PSD-95 nanoclusters was considerably weaker, and Bsn intermediate (Fig. 3d, g, Extended Data Fig. 7c–e, Supplementary Table 2). Together, both the PCFs and protein enrichment analyses revealed significant trans-synaptic alignment between RIM1/2 and PSD-95 distributions, largely stemming from the correlated positions of their respective nanoclusters. We likewise found quantitatively similar number, characteristics, and alignment of pre- and postsynaptic nanoclusters in acute hippocampal slices from adult rats (Extended Data Fig. 7f–h).

To determine whether evoked release aligns with postsynaptic receptors, we compared distributions of GluA2-containing AMPARs with RIM1/2 (Fig. 3h). Similar to PSD-95, GluA2 was significantly enriched relative to RIM1/2 nanoclusters, decaying e-fold per 66.9 ± 15.4 nm. This was further confirmed with a different GluA2/3 antibody (Supplementary Table 2). Importantly, given that the probability of AMPAR activation declines with distance from glutamate release sites has previously been deduced[3,16], we can predict synaptic potency by using the observed RIM1/2 and receptor distributions. To estimate the physiological impact of this trans-synaptic alignment, we calculated receptor activation in a measured synapse versus randomized distributions. Consistent with effect sizes posited by previous models[4,5,17], the measured distribution with trans-synaptic alignment gained 21.8 ± 0.5% in synaptic strength compared to a uniform distribution of active zone and PSD proteins (Extended Data Fig. 8), suggesting this synaptic architecture facilitates higher single-vesicle response potency. For comparison, long-term depression induces a very similar magnitude decrease in synaptic strength[18].

Notably, we found that trans-synaptic molecular alignment may extend deeper into the postsynaptic cell, as postsynaptic scaffold molecules farther from the plasma membrane also colocalized with PSD-95 nanoclusters (Extended Data Fig. 9a, c), and RIM1/2 was correspondingly enriched with respect to Shank nanoclusters (Extended Data Fig. 9b). 3D-STORM imaging of RIM1/2, PSD-95, and GKAP1 at the same synapses further confirmed their mutual co-enrichment (Extended Data Fig. 9d–f). Altogether, these results revealed an

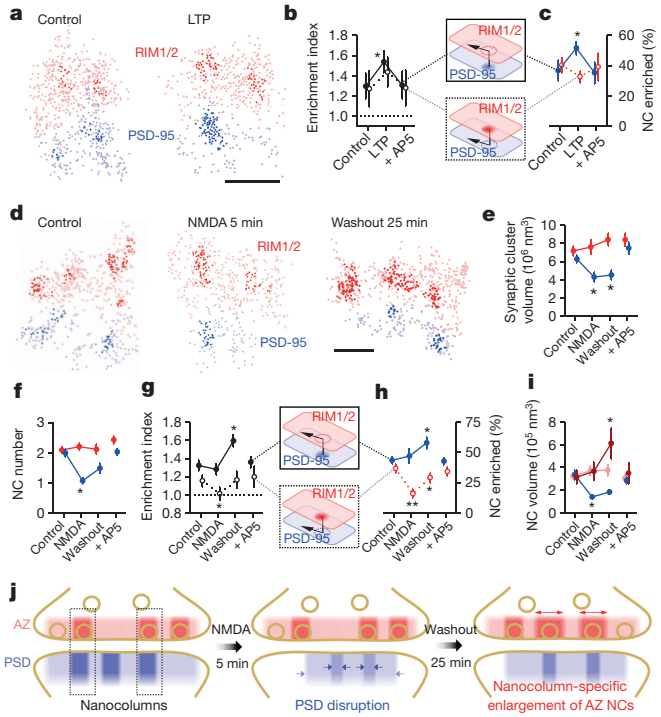

Figure 4 | Retrograde plasticity of synaptic nanoscale alignment. **a**, Distributions of synaptic RIM1/2 and PSD-95 for control and post-LTP induction conditions with nanoclusters highlighted. **b**, **c**, Across-condition comparison of enrichment index and percentage of nanoclusters enriched ($n = 45$, 87 and 42 synapses for control, LTP and AP5, respectively). **d**, Distributions of RIM1/2 and PSD-95 for conditions following NMDA stimulation. Scale bar, 100 nm. **e**–**i**, Across-conditions comparison of RIM1/2 and PSD-95. Dark red in **i** represents RIM1/2 nanoclusters enriched with PSD-95 and light red the unenriched nanoclusters. $n = 61$, 96, 77 and 74 synapses for control, NMDA, washout and AP5, respectively. **j**, Schematic summarizing the reorganization of nanoclusters during NMDA-induced plasticity and recovery. $^*P < 0.05$; $^{**}P < 0.01$, ANOVA on ranks with pairwise comparison (Dunn's method), and χ^2 test for the proportion. All experiments were repeated ≥ 3 times.

axially oriented molecular ensemble spanning the cleft within the bounds of the synapse, evoking the concept of a trans-synaptic nanocolumn enriched with key proteins that regulate synaptic transmission (Extended Data Fig. 9g). The graded protein densities involved suggest this may not be a clearly delineated structural element. Nevertheless, sensitivity of PSD-95 nanocluster size to latrunculin[4] further suggests that the spine cytoskeleton is engaged at the base of the column. Because actin executes many aspects of synaptic plasticity, this provides a potential means by which synaptic strength may be dynamically tuned.

Consequently, we speculated that nanoscale alignment might be altered during synaptic plasticity. To test this, we induced long-term potentiation via glycine stimulation and withdrawal of the NMDAR antagonist D,L-2-amino-5-phosphonovaleric acid (AP5)[19], which resulted in an increase in PSD-95 localization density within nanoclusters, in the percentage of PSD-95 nanoclusters enriched with RIM1/2, and in the enrichment index of PSD-95 nanoclusters (Fig. 4a–c, Extended Data Fig. 10m). These changes were prevented by co-application of AP5 (Fig. 4a–c, Extended Data Fig. 10m). Notably, no changes in RIM1/2 were observed, consistent with LTP as a primarily postsynaptic phenomenon.

We next tested an acute 5-min activation of NMDARs, known to induce a sustained depression of synaptic strength[20,21]. Following this stimulus, postsynaptic nanostructure was markedly disrupted in the generally opposite manner, with the synaptic cluster volume of PSD-95 and the number, volume, and protein density of PSD-95 nanoclusters all reduced (Fig. 4d–f, Supplementary Table 3). These effects were long-lasting, and during the subsequent 25 min, most parameters underwent only partial recovery. In contrast, presynaptic nanostructure underwent a remarkably different pattern of reorganization that was detectable only in relation to PSD-95 nanoclusters. Unlike PSD-95, RIM1/2 distributions were not affected immediately following the stimulus (Fig. 4d–f). However, following the 25-min recovery, the enrichment index of RIM1/2 with respect to PSD-95 nanoclusters increased with a corresponding increase in the percentage of enriched PSD-95 nanoclusters (Fig. 4g, h). Remarkably, while RIM1/2 nanoclusters altogether remained constant in number and enriched percentage, there was in fact an increase in the size of those RIM1/2 nanoclusters that were enriched with PSD-95, whereas the other non-enriched RIM1/2 nanoclusters remained constant (Fig. 4i). Similar results were found when we studied NMDA-induced changes on RIM1/2 and GluA2/3 alignment (Extended Data Fig. 10a–h). Note that on a traditional microscopic level, these changes to presynaptic organization were essentially undetectable: RIM1/2 staining revealed no change in synaptic cluster size or intensity at any point. Because the delayed presynaptic modification was specific to aligned nanoclusters, it may be that nanocolumns point to an alignment-specific, retrograde presynaptic compensation following postsynaptic depression (Fig. 4j), potentially relating to previous reports of presynaptic homeostatic plasticity[22].

Overall, the gradients of protein density we observed suggest a nanocolumn model, in which active zone regions with the highest likelihood of release are aligned to the densest receptor areas, optimizing the potency of neurotransmission (Supplementary Video 2). This provides a simple organizational principle that may hold for many small, central nervous system synapses, and will have the largest influence at synapses that typically release only one vesicle following an action potential. The compartmentalized active zone architecture is reminiscent of protein organization in *Drosophila* neuromuscular junction[23] and vertebrate ribbon synapses, where vesicles and priming proteins are arrayed around tight clusters of Ca^{2+} channels. However, observations in small central nervous system synapses of both clustered[24,25] and random distributions of Ca^{2+} channels[26], and emerging evidence for channel mobility as an equalizer of P_r for vesicles independent of channel positioning[27], suggest that their precise distribution may not be the sole determinant of the active zone release likelihood landscape.

The alignment of pre and postsynaptic nanoscale subdomains[4–6] suggests that even small synapses may be composed of dynamic functional modules[28,29]. We hypothesize that the nanocolumn represents an especially sensitive point whereby disease-associated pathways, frequently known to alter synaptic plasticity[1,2], may disrupt synapse function. It will be important to identify which, if any, of the numerous cleft-spanning adhesion systems[30] or retrograde signalling mechanisms mediate release-receptor alignment and permit dynamic trans-synaptic realignment.

Online Content Methods, along with any additional Extended Data display items and Source Data, are available in the online version of the paper; references unique to these sections appear only in the online paper.

Received 24 July 2015; accepted 27 June 2016.
Published online 27 July 2016.

1. Fromer, M. *et al.* De novo mutations in schizophrenia implicate synaptic networks. *Nature* **506,** 179–184 (2014).
2. Volk, L., Chiu, S.-L., Sharma, K. & Huganir, R. L. Glutamate synapses in human cognitive disorders. *Annu. Rev. Neurosci.* **38,** 127–149 (2015).
3. Franks, K. M., Stevens, C. F. & Sejnowski, T. J. Independent sources of quantal variability at single glutamatergic synapses. *J. Neurosci.* **23,** 3186–3195 (2003).
4. MacGillavry, H. D., Song, Y., Raghavachari, S. & Blanpied, T. A. Nanoscale scaffolding domains within the postsynaptic density concentrate synaptic AMPA receptors. *Neuron* **78,** 615–622 (2013).
5. Nair, D. *et al.* Super-resolution imaging reveals that AMPA receptors inside synapses are dynamically organized in nanodomains regulated by PSD95. *J. Neurosci.* **33,** 13204–13224 (2013).

6. Fukata, Y. *et al.* Local palmitoylation cycles define activity-regulated postsynaptic subdomains. *J. Cell Biol.* **202,** 145–161 (2013).
7. Südhof, T. C. The presynaptic active zone. *Neuron* **75,** 11–25 (2012).
8. Huang, B., Wang, W., Bates, M. & Zhuang, X. Three-dimensional super-resolution imaging by stochastic optical reconstruction microscopy. *Science* **319,** 810–813 (2008).
9. Dani, A., Huang, B., Bergan, J., Dulac, C. & Zhuang, X. Superresolution imaging of chemical synapses in the brain. *Neuron* **68,** 843–856 (2010).
10. Park, H., Li, Y. & Tsien, R. W. Influence of synaptic vesicle position on release probability and exocytotic fusion mode. *Science* **335,** 1362–1366 (2012).
11. Watanabe, S. *et al.* Ultrafast endocytosis at mouse hippocampal synapses. *Nature* **504,** 242–247 (2013).
12. Balaji, J. & Ryan, T. A. Single-vesicle imaging reveals that synaptic vesicle exocytosis and endocytosis are coupled by a single stochastic mode. *Proc. Natl Acad. Sci. USA* **104,** 20576–20581 (2007).
13. Leitz, J. & Kavalali, E. T. Fast retrieval and autonomous regulation of single spontaneously recycling synaptic vesicles. *eLife* **3,** e03658 (2014).
14. Betzig, E. Single molecules, cells, and super-resolution optics (Nobel Lecture). *Angew. Chem. Int. Ed.* **54,** 8034–8053 (2015).
15. Levet, F. *et al.* SR-Tesseler: a method to segment and quantify localization-based super-resolution microscopy data. *Nat. Methods* **12,** 1065–1071 (2015).
16. Raghavachari, S. & Lisman, J. E. Properties of quantal transmission at CA1 synapses. *J. Neurophysiol.* **92,** 2456–2467 (2004).
17. Tarusawa, E. *et al.* Input-specific intrasynaptic arrangements of ionotropic glutamate receptors and their impact on postsynaptic responses. *J. Neurosci.* **29,** 12896–12908 (2009).
18. Dudek, S. M. & Bear, M. F. Homosynaptic long-term depression in area CA1 of hippocampus and effects of *N*-methyl-d-aspartate receptor blockade. *Proc. Natl Acad. Sci. USA* **89,** 4363–4367 (1992).
19. Araki, Y., Zeng, M., Zhang, M. & Huganir, R. L. Rapid dispersion of SynGAP from synaptic spines triggers AMPA receptor insertion and spine enlargement during LTP. *Neuron* **85,** 173–189 (2015).
20. Lee, H.-K., Kameyama, K., Huganir, R. L. & Bear, M. F. NMDA induces long-term synaptic depression and dephosphorylation of the GluR1 subunit of AMPA receptors in hippocampus. *Neuron* **21,** 1151–1162 (1998).
21. Sanderson, J. L. *et al.* AKAP150-anchored calcineurin regulates synaptic plasticity by limiting synaptic incorporation of Ca^{2+}-permeable AMPA receptors. *J. Neurosci.* **32,** 15036–15052 (2012).
22. Davis, G. W. & Müller, M. Homeostatic control of presynaptic neurotransmitter release. *Annu. Rev. Physiol.* **77,** 251–270 (2015).
23. Liu, K. S. *et al.* RIM-binding protein, a central part of the active zone, is essential for neurotransmitter release. *Science* **334,** 1565–1569 (2011).
24. Holderith, N. *et al.* Release probability of hippocampal glutamatergic terminals scales with the size of the active zone. *Nat. Neurosci.* **15,** 988–997 (2012).
25. Nakamura, Y. *et al.* Nanoscale distribution of presynaptic Ca^{2+} channels and its impact on vesicular release during development. *Neuron* **85,** 145–158 (2015).
26. Scimemi, A. & Diamond, J. S. The number and organization of Ca^{2+} channels in the active zone shapes neurotransmitter release from Schaffer collateral synapses. *J. Neurosci.* **32,** 18157–18176 (2012).
27. Schneider, R. *et al.* Mobility of calcium channels in the presynaptic membrane. *Neuron* **86,** 672–679 (2015).
28. Tarr, T. B., Dittrich, M. & Meriney, S. D. Are unreliable release mechanisms conserved from NMJ to CNS? *Trends Neurosci.* **36,** 14–22 (2013).
29. Lisman, J. & Raghavachari, S. A unified model of the presynaptic and postsynaptic changes during LTP at CA1 synapses. *Sci. STKE* **2006**, re11 (2006).
30. Missler, M., Südhof, T. C. & Biederer, T. Synaptic cell adhesion. *Cold Spring Harb. Perspect. Biol.* **4,** a005694 (2012).

Supplementary Information is available in the online version of the paper.

Acknowledgements We thank S. Thompson, T. Abrams, S. Jurado and G. Wittenberg for advice and comments, P. Kaeser for advice on RIM expression and RIM antibodies, Y. Araki and R. Huganir for advice on chemLTP, and S. S. Divakaruni for advice and initial tests of chemLTP. We thank P. Kaeser for the gift of RIM1-mVenus, T. Ryan for vGlut1-pHluorin-mCherry, G. Augustine for Syn1a–CFP, and M. Contreras for technical assistance. This work was supported by F30-MH105111 to H.C., F30-MH102891 to T.P.L., F31-MH105105 to S.R.M., T32-GM008181 to H.C. and S.R.M., R01-MH080046 and NS090644 to T.A.B, and a gift from the Kahlert Foundation to T.A.B.

Author Contributions A.T. and H.C. performed STORM experiments, A.T. designed 3D-STORM analysis, H.C. performed and analysed pHuse and RIM PALM experiments, T.P.L. and A.T. performed simulations, S.R.M. performed GCaMP imaging and nanobody STORM experiments, H.D.M. performed PSD PALM experiments, and A.T., H.C. and T.A.B. designed the experiments and wrote the manuscript.

Author Information Reprints and permissions information is available at www.nature.com/reprints. The authors declare no competing financial interests. Readers are welcome to comment on the online version of the paper. Correspondence and requests for materials should be addressed to T.A.B. (tblanpied@som.umaryland.edu) or A.T. (tangaihui@gmail.com).

Reviewer Information *Nature* thanks S. Sigrist, X. Zhuang and the other anonymous reviewer(s) for their contribution to the peer review of this work.

METHODS

All experimental protocols were approved by the University of Maryland, Baltimore School of Medicine Institutional Animal Care and Use Committee. Dissociated hippocampal neurons from E18 SD rats of both sexes were prepared as described previously[31]. To increase the experiment efficiency, for three-colour STORM experiments we used the 'sandwich' cultures with a supporting astroglial monolayer as described previously[32] in which most neuronal structures were in the same focal plane. All experiments were performed on neurons 14–21 DIV and repeated on 3 or more separate cultures unless otherwise specified.

Immunostaining. Cells were fixed with 4% paraformaldehyde (PFA) and 4% sucrose in PBS (pH 7.4) for 10 min at room temperature (RT), followed by washing with 50 mM glycine in PBS. Cells were then permeabilized and blocked using 3% BSA or 5–10% donkey or goat serum in PBS with 0.1% Triton X-100, followed by incubation with primary antibody (3 h RT or 4 °C overnight) and secondary antibodies (1 h RT).

For comparisons of Munc13 or RIM1/2 with Bsn made using 3D-STORM, mouse anti-Bsn (1:500, Enzo) was used with either rabbit anti-RIM1/2 (1:500; Synaptic Systems No. 140203) or rabbit anti-Munc13 (1:500; Synaptic Systems No. 126103). Cy3 or Alexa-647 conjugated goat or donkey anti-rabbit or anti-mouse secondary antibodies (1:200 in PBS; JacksonImmuno) were used[33]. For comparisons of Munc13 and RIM1/2, staining was performed sequentially separated by additional blocking steps of incubation with rabbit serum at RT for 30 min followed by incubation with excess unconjugated anti-rabbit Fab antibody for 1 h at RT. For this set of experiments, all permutations of the order in which the primary antibody was applied and the fluorophore used to label each protein were included. For trans-synaptic measurements, rabbit anti-Munc13, anti-RIM1/2, anti-RIM1 (1:500; Synaptic Systems No.140003) or anti-Bsn (1:500, Cell Signaling), were used with mouse anti-PSD-95 (1:200; Neuromab), mouse anti-GluA2 (1:100, Millipore), or rabbit anti-GluR2/3 (1:100, Millipore). Unless specified otherwise, presynaptic proteins were labelled with donkey anti-rabbit IgG conjugated with Alexa-647 and postsynaptic PSD-95 were labelled with donkey anti-mouse IgG conjugated with Cy3. For comparison of directly labelled primary antibody with primary–secondary antibody labelling, we directly conjugated Alexa-647 dye to anti-PSD-95 antibody and purified antibody using illustra NAP Columns (GE Healthcare). For comparison of nanobody labelling of expressed GFP-tagged knockdown-rescue PSD-95 with primary–secondary antibody labelling, we used GFP-booster (1:200, Chromotek). More information on antibodies used can be found in the Supplementary Information.

Tissue slice staining was performed essentially as previously described[9,34]. Briefly, 1-mm thick blocks of hippocampal tissue from 5–7-week-old male SD rats were fixed with ice-cold 4% PFA for 15 min and then dehydrated with 30% sucrose in PBS. Cryostat sections with 40 μm thickness were made, permeabilized and blocked with 10% donkey serum and 0.3% Triton X-100 in PBS/glycine for 1 h. PSD-95 and RIM1/2 were labelled with the same antibody concentration as was used in cell culture.

3D-STORM imaging. Imaging was performed on an Olympus IX81 ZDC2 inverted microscope with a 100×/1.49 TIRF oil-immersion objective. Excitation light was reflected to the sample via a 405/488/561/638 quad-band polychroic (Chroma). The typical incident power was ~30 mW for 647 nm and ~60 mW for 561 nm (measured through the objective). To reduce background fluorescence while maximizing the depth of view, we adjusted the incident angle of the excitation beam to near but less than the critical angle, to achieve oblique illumination of the sample. Emission was passed through a Photometrics DV2 which split the emission at 565 nm and directed the red and far-red bands through matched filters (595/50 and 655 long-pass) onto an iXon+ 897 EM-CCD camera (Andor). A cylindrical lens (focal length = 30 cm) was inserted in each path of the splitting cassette of the DV2 to create the astigmatism for 3D imaging. All hardware was controlled via iQ software (Andor). *Z* stability was maintained by the Olympus ZDC2 feedback positioning system. Lateral drift was corrected with a cross-correlation drift-correction approach[35,36].

Labelled cells and tissue slices were imaged in a STORM imaging buffer freshly made before experiments containing 50 mM Tris, 10 mM NaCl, 10% glucose, 0.5 mg/ml glucose oxidase (Sigma), 40 μg/ml catalase (Sigma), and 0.1 M cysteamine (Sigma). For tissue slices, the focal plane was set to within 1.5 μm from the glass coverslip to obtain the best signal-to-noise ratio. Imaging was performed as previously described[4,33]. TetraSpeck beads (100 nm; Invitrogen) deposited on a coverslip were localized to correct alignment between the two channels as described previously[4]. The average deviation of the bead localizations after correction was between 10 and 15 nm. To calibrate the 3D positions of localizations, a *z*-stack with 30-nm steps was collected on the same coverslip with beads. The average deviation of localized *z*-positions of immobilized fluorophores was 40–50 nm.

Three-colour 3D-STORM. Three-colour STORM were performed with two sequential sets of two-colour 3D-STORM on RIM1/2-PSD-95 as a pair and then GKAP1-PSD-95 as a pair. Cells were immunolabelled with mouse anti-PSD-95, rabbit anti-RIM1/2, and mouse anti-GKAP1 (1:200, Neuromab). PSD-95 and RIM1/2 were then immunolabelled with secondary antibodies conjugated to Alexa647 and Cy3, respectively. After >20 min of continuous excitation by high-powered lasers during the first round of imaging, the majority of Cy3 molecules (RIM1/2) became bleached. After acquisition of the first set of data, GKAP1 was then labelled with secondary antibody conjugated to Cy3 while the coverslip remained on the microscope. The two sets of data were aligned post hoc based on Alexa647 (PSD-95) localizations. Because RIM1/2 and GKAP1 are not overlapping proteins, in the second imaging set, those Cy3 localizations within the RIM cluster borders potentially arising from the small, unbleached fraction of RIM-Cy3 were rejected from GKAP1 localizations.

PALM-STORM Imaging. PALM imaging of PSD-95 concurrent with STORM imaging of GKAP or Shank (1:200, Neuromab) was performed as previously described[4].

Single-molecule localization and analysis. All data analysis was performed offline using custom routines in MATLAB (Mathworks). Molecule locations were determined by fitting an elliptical 2D Gaussian function to an 11 × 11 pixel array (pixel size 100 nm) surrounding the peak[4]. The lateral (*x*, *y*) and axial (*z*) coordinates of the fluorophore were determined from the centroid position and ellipiticity of the fitted peak, respectively[8]. Only molecules localized with an *x*–*y* precision <10 nm (ref. 37), fitting $R^2 > 0.6$, and comprising >200 photons were used for further analysis.

To remove the localizations from those fittings of multiple overlapping peaks, we developed a rejection criteria based on the shape of peaks. For peaks arising from single fluorophores, the fitted width in *x* and *y* (W_x and W_y, respectively) should correlate in a manner mainly determined by the cylindrical lens. All localizations away from this correlation would come from multiple overlapping or poorly fitted peaks and were therefore rejected (Extended Data Fig. 1a–f).

Single-molecule tracking was employed to remove the overcounted localizations from peaks lasting for more than one frame. Tracking was accomplished with available algorithms (http://physics.georgetown.edu/matlab/). Particles appearing in consecutive frames separated by no more than 200 nm were collapsed into one track and considered one molecule by taking only the location in the first frame for further analysis.

Analysis of synaptic clusters. A potential synapse could be identified by a juxtaposed pair of synaptic proteins in a 2D scatter plot of all accepted localizations from both channels. By rotating a 3D scatter plot of localizations of a selected potential synapse, we evaluated the data quality and selected only those with clear pre- and postsynaptic components (for example, no nearby third cluster which may indicate two synapses in close proximity) for further analysis. To define the border of a synaptic cluster, the nearest neighbour distances (NND) between localizations were calculated and the mean + 2 s.d. of NND was used as a cut-off to divide the localizations into sub-clusters. All localizations outside of the primary sub-clusters were considered to be background and discarded.

Owing to the irregularly curved shapes of some synapses, using the convex hull to define synaptic cluster shape would overestimate the synaptic cluster volume. We thus defined the synaptic cluster using the alpha shape of the set of 3D localizations with $\alpha = 150$ nm. This value was determined based on series of tests on >100 synapses to obtain the best synaptic cluster shape while avoiding dramatic changes in volume when individual localizations near the border were added or removed. This alpha shape algorithm gave a synaptic cluster volume of 81 ± 3% of the convex hull volume ($n = 156$ synapses). Subsequently, this alpha shape was used as the cluster border when localizations were randomized.

A synaptic cluster was only considered for analysis if the volume was between 2×10^{-3} μm^3 and 30×10^{-3} μm^3 (ref. 38), and contained an average density of $>8 \times 10^3$ localizations/μm^3. Local density was defined as the number of molecules within a radius of 2.5 times the standard median nearest neighbour distance (MdNND) for the synaptic cluster density. The standard MdNND was calculated from a standard correlation curve $\mathrm{MdNND} = \sqrt[3]{\frac{0.174}{d}}$ (unit per 100 nm voxel for *d*) where *d* is the averaged localization density. This equation is derived from fitting MdNND with *d* in a series of simulations of uniformly distributed synaptic clusters with different densities. The reason we used this standard MdNND instead of the median NND from the original synaptic cluster was to reduce the deviation caused by local assembles.

Nanocluster analysis. Localizations with local densities ≥14 were selected and divided into agglomerative sub-clusters with a node height cut-off of 40 nm using MATLAB functions linkage() and cluster(). For each sub-cluster, we then calculated the NND and discarded those localizations with NND > MdMND if any. Only those sub-clusters containing ≥4 localizations were counted as nanoclusters.

These criteria were chosen based on a conservative strategy such that no nanoclusters were identified in simulations of randomly distributed synaptic clusters

with different densities. Consequently, they may have prevented detection of small or weakly enriched nanoclusters. In principal, we cannot completely exclude the possibility of overcounting, so a certain fraction of detected nanoclusters are potentially artificial. However, we used the same standard on all data sets. Since all the trans-synaptic analyses were well controlled by randomizing simulations, this contamination is not able to produce false positives for trans-synaptic alignment analyses. On the contrary, it may attenuate the significance of the differences in trans-synaptic analyses based on nanoclusters, including cross-correlation, protein enrichment and the fraction of enriched nanoclusters.

Since the number of localizations in one nanocluster was typically small, using convex hull or alpha shape would greatly under-estimate the nanocluster volume due to the border effect. Therefore, we tessellated the synaptic cluster with polyhedrons using MATLAB function voronoin(), with each Voroni cell containing one localization. The nanocluster volume was calculated as a summation of volumes of all polyhedrons containing the nanocluster localizations. To avoid unexpected unbounded Voronoi cells and over-estimating the volume of cells near the cluster surface, we introduced ~10% background noise by adding randomly distributed localizations around the cluster[15]. Polyhedron volume for each localization was averaged across ten independent simulations.

ACF analysis. To quantify the self-clustering of synaptic proteins, we adapted an autocorrelation function[4,39] for our 3D data. The autocorrelation function $g_a(r)$ is a measure of density correlations, which reports increased probability of finding a second localized signal a distance r away from a given localized signal. It was tabulated in Matlab using Fast Fourier Transforms (FFTs), as in equation (1).

$$g_a(\vec{r}) = \frac{\mathrm{FFT}^{-1}(|\mathrm{FFT}(\boldsymbol{I})|^2)}{\rho^2 \mathrm{FFT}^{-1}(|\mathrm{FFT}(W)|^2)} \quad (1)$$

FFT^{-1} is an inverse Fast Fourier Transform, $\boldsymbol{I}$ is the reconstructed 3D density matrix of localized fluorophores (pixel size of 5 nm), ρ is the general localization density inside the synaptic cluster, and W is a shape function that has the value of 1 inside the synaptic cluster as defined above with an alpha shape and the value of 0 elsewhere. The matrix $\boldsymbol{I}$ was padded with zeros in all three directions out to a distance larger than the range of the desired correlation function (we used 200 nm) to avoid artefacts due to the periodic nature of FFT functions. W was also padded by an equal number of zeros. $\mathrm{FFT}^{-1}(|\mathrm{FFT}(W)|^2)$ is a normalization factor accounting for the general shape of the synaptic cluster itself so that the output of the $g_a(\vec{r})$ represented only the internal structure of the measured synaptic cluster. $g_a(\vec{r})$ was symmetric to rotations around the centre of matrix $\boldsymbol{C}$ (x_c, y_c, z_c), and it could be averaged over angles to obtain $g_a(r)$ by converting to polar coordinates. $g_a(r)$ was then binned by radius (r). Correlation functions were plotted for $r > 0$, as $g_a(r = 0)$ was a trivial contribution.

For a uniform distribution, for example, when all localizations were uniformly randomized within the alpha shape, $g_a(r) = 1$ (Fig. 1d). Any heterogeneity will result in a $g_a(r) > 1$. The extent of $g_a(r)$ over 1, that is, r_0 for $g_a(r_0) = 1$, is related to the pattern size of the internal heterogeneity (Extended Data Fig. 2b, c)[39].

Isolated, non-synaptic small groups of localizations were taken from our experimental data. These localization groups likely represent an overestimate of a single-dye-molecule localization spread. Nevertheless, we find that they are still significantly smaller than the large majority of the nanoclusters we detected.

Imaging vesicle exocytosis. For imaging vesicle fusion, vGluT-pHluorin-mCherry (a gift from T. Ryan)[40,41], was cotransfected with Syn1a–CFP (a gift from G. Augustine) using Lipofectamine 2000 (Invitrogen) for 4–6 days before imaging cells at 14–20 DIV. Optical measurements were performed using a laminar-flow perfusion and stimulation chamber. Images were acquired at 10 Hz with an Andor iXon 887 EM-CCD camera on an Olympus IX81 ZDC2 inverted microscope with a 100×/1.49 TIRF oil-immersion objective. Temperature was controlled using an objective heater set at either room temperature (~25 °C) or 32 °C. Action potentials were evoked by passing 1 ms current pulses yielding fields of ≈10 V/cm via platinum-iridium electrodes. Terminals were selected for imaging by assessing their responsiveness, as indicated by a fluorescence increase, to a 10 AP train at 20 Hz. A wide-field Syn1a image was then taken at the imaging plane. Single AP-evoked release was measured over 60 trials of (1) 1 s acquisition of baseline fluorescence, (2) stimulus, (3) 2.5 s acquisition of post-stimulus fluorescence, (4) 7 s recovery during which the laser is off. Spontaneous release was measured over 5 min of continuous acquisition. Cells were imaged in a saline solution containing 120 mM NaCl, 3 mM KCl, 2 mM $CaCl_2$, 2 mM $MgCl_2$, 10 mM glucose, and 10 mM HEPES, pH adjusted to 7.4 with NaOH, 10 μM 6,7-dinitroquinoxaline-2,3-dione (DNQX; Sigma), 50 μM D,L-2-amino-5-phosphonovaleric acid (AP5; Sigma), and 500 nM Jasplikinolide (Jasp; Millipore) at room temperature (~25 °C). When higher [$CaCl_2$] was used, [$MgCl_2$] was reduced to keep the divalent ion concentration constant. For measurements of spontaneous events, 500 nM tetrodotoxin (TTX; Enzo) was added after identifying terminals using AP-evoked fluorescence increase.

For calculating normalized changes in fluorescence ($\Delta F/F$), images were analysed in ImageJ by custom-written plugins[12]. Average fluorescence intensities were measured over a circular region of interest (ROI) of radius 800 nm for each bouton. Change in fluorescence (ΔF) was calculated as the difference in intensity of the frame after the stimulus was delivered and the average ROI intensity of 5 baseline frames not including the first frame or the frame immediately before the stimulus (F_{baseline}). $\Delta F/F$ was calculated by normalizing each ΔF to F_{baseline}.

pHuse localization and analysis. Data analysis was performed offline using custom routines in MATLAB (Mathworks). Boundaries for individual boutons were determined using wide-field images of Syn1a–CFP centred at the focal plane of the pHuse experiments thresholded at 50% of the peak intensity (33% and 67% thresholds were also compared and showed no significant difference on the effect of mode of release, shown in Extended Data Fig. 5i). Binary images were created from the thresholded image, and Syn1a–CFP puncta area calculated as a measure of bouton area, which correlated with pHuse area, as expected[42]. Images for each fusion event were processed using frame-by-frame subtraction followed by background subtraction to isolate fluorescence increases (Fig. 2d)[43]. Similar detection thresholds were set for spontaneous (75 ± 15) and evoked (78 ± 14, $t = 0.88$, $P = 0.40$) release, at ~3–4 times above background noise, on an individual imaging field basis. Spatial localization of the fusion events was determined by fitting an elliptical 2-dimensional Gaussian function to a 9×9 pixel array surrounding the peak. Only molecules localized with a precision < 25 nm[37,44], elliptical form < 1.3, and comprising > 100 photons were used for further analysis. An additional criterion to exclude evoked pHuse localizations with photon counts > mean + 2 s.d. of spontaneous photon count distribution was used in Extended Data Fig. 5d and showed no significant difference compared to the distribution lacking this criterion. Localizations from multiple fusion events over time at individual boutons were mapped. A 2D convex hull algorithm was used to calculate the minimal convex polygon that incorporated all fusion site localization points. The area of the resulting polygon was used as the fusion site (pHuse) area.

Photon count distributions analysis. Data analysis was performed offline using custom routines in MATLAB (Mathworks). The distribution for spontaneous fusion events was fit with a normal distribution using normfit(), which uses maximal likelihood estimation for optimization. The distribution of evoked fusion events was fit with a custom univariate distribution for a mixture of two normal distributions with a probability density function (pdf) defined in equation (2). This fitting also used maximal likelihood estimation for optimization of five parameters, including the mixture probability (p), and the population means (μ_1, μ_1) and variance (σ_1, σ_2) for each component, over 300 iterations using normpdf() to compute the pdf for each of the two component normal distributions.

$$\mathrm{pdf} = p \times \mathrm{normpdf}(x, \mu_1, \sigma_1) + (1 - p) \times \mathrm{normpdf}(x, \mu_2, \sigma_2) \quad (2)$$

Here p was constrained between 0 and 1, and σ had a lower bound of 0. This mixture probability defined the lower estimate (72%) for the percentage of single stimulus evoked fusion arising from single vesicles. We calculated the higher estimate (82%) by calculating the percentage of evoked fusion events with photon counts within two standard deviations of the mean spontaneous fusion event photon count. To assess the influence of multivesicular events on evoked pHuse area, we used this as a cut-off to exclude localizations above this photon count. We found no significant difference between evoked area with and without excluding these events (Extended Data Fig. 5d).

Ca^{2+} imaging and analysis. For Ca^{2+} imaging, the genetically encoded indicator GCaMP6f (ref. 45) was transfected at 14 DIV and imaged 3 days after transfection. GCaMP6f was used to detect postsynaptic miniature spontaneous Ca^{2+} transients (mSCaTs) that arose in dendritic spines following NMDA receptor activation by spontaneous release[46]. Coverslips were placed in custom-made chambers in saline solution containing 1 μM TTX, 10 μM DNQX, 25 μM picrotoxin (Sigma), and 5 μM nifedipine (Sigma). Imaging was performed on a spinning disk confocal system (Andor Technology), consisting of a CSU-22 confocal (Yokagawa) with a Zyla 4.2 CCD camera detector (Andor) mounted on the side port of an Olympus IX-81 inverted microscope, using a 60×/1.42 oil-immersion objective, yielding a final effective pixel size of 108 nm. Continuous acquisition at 20 Hz was collected for 3 min, controlled by iQ software (Andor).

Data analysis was performed offline using custom routines in Metamorph (Molecular Devices), Clampex (Molecular Devices), and Matlab (Mathworks). First, using Metamorph, a baseline image was created by averaging the first three and last three image frames and a maximum intensity projection was made by averaging all image frames. Image subtraction of the baseline from the maximum intensity projection revealed spines that showed an increase in GCaMP intensity. Regions of interest (ROIs) were drawn around these 'active' spines as well

as a background region and then transferred to the original timelapse. For each ROI the averaged intensity was measured per frame. The average intensity of the background ROI was subtracted from the average intensity of 'active' spine ROIs. From this, an average fluorescence intensity was calculated for every 10 frames, and within every minute interval of imaging the lowest positive value was used as the baseline fluorescence intensity for that minute ($F_{\text{baseline,1 min}}$). A normalized change in fluorescence ($\Delta F/F$) was calculated for each frame as $(F_{\text{frame}} - F_{\text{baseline,1 min}})/F_{\text{baseline,1 min}}$. The $\Delta F/F$ values were then fed into Clampex, and mSCaTs were detected using a template search that identified peaks based on a shape profile determined from mSCaT examples with near-average rise and decay time courses.

Confocal imaging of presynaptic proteins. Neurons 14–20 DIV were cotransfected for 3 days with RIM1-mVenus (a gift from P. Kaeser) and Syn1a–CFP to assess colocalization. Neurons transfected with only RIM1-mVenus were immunostained with chicken anti-GFP (1:200, Chemicon) labelled with secondary anti-chicken-Alexa-488, rabbit anti-RIM1/2 labelled with secondary anti-rabbit-Cy3, and mouse anti-Bsn labelled with secondary anti-mouse-Alexa-647 to assess expression levels. Imaging was performed on a spinning disk confocal system as described above. ImageJ was used to analyse fluorescence intensity of RIM1/2 and Bsn at transfected compared to neighbouring untransfected boutons.

PALM-pHuse. RIM1-mEos3.1 was constructed by subcloning mEos3.1 from mEos3.1-N1 (a gift from S. McKinney) into pCMV5-RIM1-mVenus (P. Kaeser) in place of mVenus at NotI-AscI. PALM was performed on RIM1, and nanoclusters identified using local density measured by nearest neighbour distance as previously described[4], or using an adapted form of SR-Tesseler first rank neighbour density (δ^1), using 2× mean δ^1 of the whole synapse as the threshold for identifying nanoclusters, as described in ref. 15. Nanoclusters identified by both methods were similar in size (Extended Data Fig. 6). To map vesicle fusion to active zone nanostructure, RIM1-mEos3.1 was cotransfected with vGpH at 10–14 DIV and imaged at 14–18 DIV. RIM1 PALM and pHuse of 1-AP-evoked release was performed as described above sequentially on the same boutons. Overlapping RIM1 and pHuse localizations were analysed at boutons containing >10 RIM1 localizations and >3 pHuse localizations offline using custom routines in MATLAB (Mathworks). vGpH fluorescence increase following a 10 AP-train stimulus was used to outline the border of individual boutons. Randomized distributions of RIM1 were simulated for each synapse by randomly placing the same number of RIM1 localizations within the same area of RIM1 as calculated by convex hull of the measured RIM1 distribution. RIM1 local density within these randomized distributions was similarly calculated. Normalized RIM1 δ^1 was calculated with respect to overall synaptic localization density.

3D paired cross-correlation function (PCF) analysis. The 3D PCF was adapted from a similar function previously used to quantify colocalization in 2D data[39]. It was computed using two matrices ($\boldsymbol{I}_1$ and $\boldsymbol{I}_2$) reconstructed from two image channels (equation (3).

$$g_c(\vec{r}) = \mathrm{Re}\left\{\frac{\mathrm{FFT}^{-1}(FFT(\boldsymbol{I}_1) \times \mathrm{conj}[\mathrm{FFT}(\boldsymbol{I}_2)])}{\rho_1\rho_2 \mathrm{FFT}^{-1}(\mathrm{FFT}(W_1) \times \mathrm{conj}[\mathrm{FFT}(W_2)])}\right\} \quad (3)$$

Here, conj[] is a complex conjugate, ρ_1 and ρ_2 are the averaged localization densities in the pair of synaptic clusters, W_1 and W_2 are shape functions of the two synaptic clusters, and Re{} indicates the real part. Different from the ACF, the symmetric origin of $g_c(\vec{r})$ here is no longer the matrix centre $C(x_c, y_c, z_c)$, but a different point $A(x, y, z)$, and the vector $\overrightarrow{CA}$ represents the direction and distance for the translation of PSD-95 synaptic clusters ($\boldsymbol{I}_2$) to get the best overlap with presynaptic clusters ($\boldsymbol{I}_1$). We computed the direct correlation between $\boldsymbol{I}_1$ and $\boldsymbol{I}_2$ with equation (4).

$$G = \mathrm{FFT}^{-1}(\mathrm{FFT}(\boldsymbol{I}_1') \times \mathrm{conj}[\mathrm{FFT}(\boldsymbol{I}_2')]) \quad (4)$$

A is the point with the peak G value. Because the originally constructed matrices $\boldsymbol{I}_1$ and $\boldsymbol{I}_2$ were not continuous, to reduce the noise of the correlation, we first convoluted the two matrixes with an $11 \times 11 \times 11$ kernel (Extended Data Fig. 1g). To avoid having the correlation be dominated by local domains with high localization density, we cut the peaks of the convoluted matrixes to 1/4 of the mean localization density within synaptic clusters ($\rho_1/4$ and $\rho_2/4$) (Extended Data Fig. 1h) so that G only represented the relationship between the general 3D shapes of the two synaptic clusters ($\boldsymbol{I}_1', \boldsymbol{I}_2'$) without internal heterogeneity (Extended Data Fig. 1m, n). Around A, $g_c(\vec{r})$ is symmetric and could be angularly averaged to get $g_c(r)$.

Since the information of synaptic cluster shape and overall density had been normalized, $g_c(r)$ was fully dependent on the internal organizations of the two synaptic clusters. If localization assemblies inside the two synaptic clusters organized in a similar pattern and opposed each other, $g_c(r) > 1$. If either synaptic cluster had a uniform distribution of localizations (Fig. 3b) or the internal assemblies were not aligned (Fig. 3c), $g_c(r) = 1$. Different from the ACF, overcounting has no effect on the PCF[39].

Protein enrichment analysis. The protein enrichment profile of protein A relative to a protein-B nanocluster, $E_{A\to B}(r)$, was calculated as the angularly averaged localization density of protein A around the aligned centre of a protein-B nanocluster normalized to the average localization density in synaptic cluster A. The aligned nanocluster centre was found as shown in Extended Data Fig. 1. To avoid potential problems caused by boundary conditions, we calculated the enrichment profile as equation (5).

$$E_{A\to B}(r) = \frac{N_{A\to B}(r)}{N_{A_r(m)\to B}(r) \times m} \quad (5)$$

$N_{A\to B}(r)$ is the binned distribution of protein-A localization number to the aligned protein-B nanocluster centre, $N_{A_r(m)\to B}(r)$ is the distribution of localization number for a uniformly randomized synaptic cluster A with m times of original localization density, and m is a factor set to 15 to reduce the effect of fluctuations. A protein-B nanocluster was considered to be significantly enriched with protein A if $E_{A\to B}(r) > \mathrm{mean}[E_{A_r\to B}(r)] + 1.96 \times \mathrm{standarddeviation}[E_{A_r\to B}(r)]$, where $E_{A_r\to B}(r)$ represents the enrichment profile of ten simulated uniformly randomized A synaptic clusters with the original density and the same alignment to the nanocluster centre of protein-B.

Chemical LTP and LTD. Chemical LTP was performed using a combination of AP5 withdrawal and application of glycine as described in ref. 19. Briefly, 3–4-week-old cultures were treated with 200 μM DL-AP5 in culture medium for two days and then transferred to ACSF (150 NaCl, 3 KCl, 2 $CaCl_2$, 1 $MgCl_2$, 10 HEPES-Na, 10 D-glucose, all in mM, pH 7.4) with 100 μM picrotoxin, 1 μM strychnine, 0.5 μM TTX and 200 μM AP5. After preincubation for 1–2 h, chemical LTP was induced with 15 min incubation in the similar solution with 200 μM glycine but without Mg^{2+} and AP5. Neurons were fixed directly following induction. Chemical LTD was performed using application of NMDA as described in ref. 20. Control solutions of regular saline solution or co-application with AP5 were paired with experimental conditions. Cells were fixed either immediately after plasticity induction or washed with saline and incubated for 25 min at 37 °C to allow recovery before fixing. Cells were then immunostained and imaged as described above.

Synaptic modelling. We used an experimentally constrained deterministic approach to study the dependence of synaptic strength on the spatial distribution of release sites and AMPARs. Central to this approach is the relationship between channel opening probability and its distance from a release site, determined previously by stochastic modelling approaches[3,16,47]:

$$P_o(r) = 0.42\ \mathrm{e}^{-r/88} \quad (6)$$

where r is the lateral distance between an AMPAR and a release site (in nm). In brief, the distribution of RIM1/2 proteins and GluA2/3-containing AMPA receptors measured by STORM were used to determine the spatial coordinates of release sites and AMPARs on a model synapse. Since the precise photophysics and blink distribution of dyes are complicated and the exact efficiency of antibody labelling is unknown, we calculated gradient maps of spatial coordinates to determine putative RIM1/2 protein and AMPAR locations from the single-molecule images. First, the 3D spatial coordinates were projected onto 2D planes orthogonal to the manually determined axodendritic axis. Each projected point was assigned a Gaussian function, the amplitude and width of which were determined by the normalized local density and the lateral STORM localization precision (20 nm). Overlapping Gaussian functions within the active zone or PSD convex hull were integrated to create the pre- and postsynaptic gradient maps. The sampling pixel size was 2.5 nm (the calculated synaptic response was independent of pixilation level for sampling size from 1 to 20 nm, data not shown). The pre- and postsynaptic gradient maps were separated by 20 nm, the cleft distance used to determine equation (6)[3].

The model synaptic response for a single synapse was computed as the expected fraction of receptors that would open given a single release, averaged over all possible release locations in the active zone. For any single release event, the expected open fraction of channels at the peak of the response was calculated as follows:

$$O(i) = \sum_j \left[P_o(r_{ij}) \frac{\mathrm{LD}_j}{\sum_j \mathrm{LD}_j}\right] \quad (7)$$

where r_{ij} is the lateral distance between the ith pixel in the presynaptic gradient map and the jth pixel in the postsynaptic gradient map; the expected fraction of open channels $O(i)$ from the ith release site is sum of channel opening probabilities at all pixels in the postsynaptic gradient map, where each jth pixel is weighted by

its normalized local density LD_j (that is, the channel fraction is assumed to be directly proportional to the channel local density). To constrain the location of release events in the active zone, we used the live-cell pHuse-PALM data, which showed that release events preferentially occurred in regions with normalized RIM local density greater than 1.5, and these events occurred over 20–60% of the active zone area (spontaneous pHuse area/PALMed RIM area, and evoked pHuse area/spontaneous pHuse area). To account for these measured features, we modelled the spatial likelihood of release as a piecewise sigmoidal function dependent on the normalized local RIM density:

$$P_r(i \mid \text{release}) = \begin{cases} 0.5\left[\dfrac{(1-s)^{\frac{LD_i}{LD_{inflect}}}}{2-s-\frac{LD_i}{LD_{inflect}}}\right] & \text{if } LD_i \in [0, LD_{inflect}] \\ 0.5+0.5\left[\dfrac{(1-s)^{\frac{LD_i-LD_{inflect}}{LD_{max}-LD_{inflect}}}}{2-s-\frac{LD_i-LD_{inflect}}{LD_{max}-LD_{inflect}}}\right] & \text{if } LD_i \in [LD_{inflect}, LD_{max}] \end{cases} \quad (8)$$

where s is the steepness of the sigmoid transition, LD_i is the normalized local density of RIM at the ith pixel of the presynaptic gradient map, $LD_{inflect}$ is the point of inflection in the sigmoidal function, and LD_{max} is the maximum normalized local density of RIM in the STORM measured example shown in Extended Data Fig. 8b. $LD_{inflect}$ and s were fitted to be 1.5 and 0.959 in order to yield a fractional release area of 40%. To calculate the average peak synaptic response per release, we calculated the expected open channel fraction averaged over all possible release sites weighted by the spatial probabilities of release:

$$\text{Open channels at peak response } (\%) = \sum_i \left[O(i) \frac{P_r(i \mid \text{release})}{\sum_i P_r(i \mid \text{release})} \right]$$

Code availability. All code used in the paper is available upon request.

Statistical analysis. No statistical methods were used to predetermine sample size. The experiments were not randomized, and investigators were not blinded to allocation during experiments and outcome assessment. Statistical tests were performed with Sigmastat, MATLAB, Graphpad, or R. No statistical methods were used to predetermine sample size. The sample sizes were determined based on numbers reported in previous studies. For comparison of two or more distributions, all samples were assessed for normality using Shapiro–Wilk or Kolmogorov–Smirnov tests. If samples met criteria for normality, we used a Student's t-test to compare two groups, a paired t-test for comparison of the same group before and after a treatment, or ANOVA for more than two groups. If ANOVAs were significant, we used a post hoc Tukey test to compare between groups. For groups with combinations of discrete and continuous variables, we used MANCOVAs. We only performed two-tailed tests. Homogeneity of variances was tested using an F-test and found to be similar between compared groups. If samples did not meet criteria for parametric tests, we used Kolmogorov–Smirnov or Wilcoxon rank-sum tests for comparison of two groups and Kruskal–Wallis or Friedman ANOVA for comparison of more than two groups, with post hoc analysis using Dunn's test. Data are presented as mean ± s.e.m. unless otherwise specified. Also see Supplementary Tables.

31. Frost, N. A., Shroff, H., Kong, H., Betzig, E. & Blanpied, T. A. Single-molecule discrimination of discrete perisynaptic and distributed sites of actin filament assembly within dendritic spines. *Neuron* **67,** 86–99 (2010).
32. Kaech, S. & Banker, G. Culturing hippocampal neurons. *Nat. Protocols* **1,** 2406–2415 (2006).
33. van de Linde, S. *et al.* Direct stochastic optical reconstruction microscopy with standard fluorescent probes. *Nat. Protocols* **6,** 991–1009 (2011).
34. Schneider Gasser, E. M. *et al.* Immunofluorescence in brain sections: simultaneous detection of presynaptic and postsynaptic proteins in identified neurons. *Nat. Protocols* **1,** 1887–1897 (2006).
35. Geisler, C. *et al.* Drift estimation for single marker switching based imaging schemes. *Opt. Express* **20,** 7274–7289 (2012).
36. Mlodzianoski, M. J. *et al.* Sample drift correction in 3D fluorescence photoactivation localization microscopy. *Opt. Express* **19,** 15009–15019 (2011).
37. Thompson, R. E., Larson, D. R. & Webb, W. W. Precise nanometer localization analysis for individual fluorescent probes. *Biophys. J.* **82,** 2775–2783 (2002).
38. Schikorski, T. & Stevens, C. F. Quantitative ultrastructural analysis of hippocampal excitatory synapses. *J. Neurosci.* **17,** 5858–5867 (1997).
39. Veatch, S. L. *et al.* Correlation functions quantify super-resolution images and estimate apparent clustering due to over-counting. *PLoS One* **7,** e31457 (2012).
40. Kim, S. H. & Ryan, T. A. CDK5 serves as a major control point in neurotransmitter release. *Neuron* **67,** 797–809 (2010).
41. Voglmaier, S. M. *et al.* Distinct endocytic pathways control the rate and extent of synaptic vesicle protein recycling. *Neuron* **51,** 71–84 (2006).
42. Harris, K. M. & Stevens, J. K. Dendritic spines of CA 1 pyramidal cells in the rat hippocampus: serial electron microscopy with reference to their biophysical characteristics. *J. Neurosci.* **9,** 2982–2997 (1989).
43. Simonson, P. D., Rothenberg, E. & Selvin, P. R. Single-molecule-based super-resolution images in the presence of multiple fluorophores. *Nano Lett.* **11,** 5090–5096 (2011).
44. Thompson, M. A., Lew, M. D. & Moerner, W. E. Extending microscopic resolution with single-molecule imaging and active control. *Annu. Rev. Biophys.* **41,** 321–342 (2012).
45. Chen, T.-W. *et al.* Ultrasensitive fluorescent proteins for imaging neuronal activity. *Nature* **499,** 295–300 (2013).
46. Murthy, V. N., Sejnowski, T. J. & Stevens, C. F. Dynamics of dendritic calcium transients evoked by quantal release at excitatory hippocampal synapses. *Proc. Natl Acad. Sci. USA* **97,** 901–906 (2000).
47. Xie, X., Liaw, J.-S., Baudry, M. & Berger, T. W. Novel expression mechanism for synaptic potentiation: alignment of presynaptic release site and postsynaptic receptor. *Proc. Natl Acad. Sci. USA* **94,** 6983–6988 (1997).
48. Kavalali, E. T. *et al.* Spontaneous neurotransmission: an independent pathway for neuronal signaling? *Physiology (Bethesda)* **26,** 45–53 (2011).
49. Frank, T. *et al.* Bassoon and the synaptic ribbon organize Ca^{2+} channels and vesicles to add release sites and promote refilling. *Neuron* **68,** 724–738 (2010).
50. Ermolyuk, Y. S. *et al.* Differential triggering of spontaneous glutamate release by P/Q-, N- and R-type Ca^{2+} channels. *Nat. Neurosci.* **16,** 1754–1763 (2013).

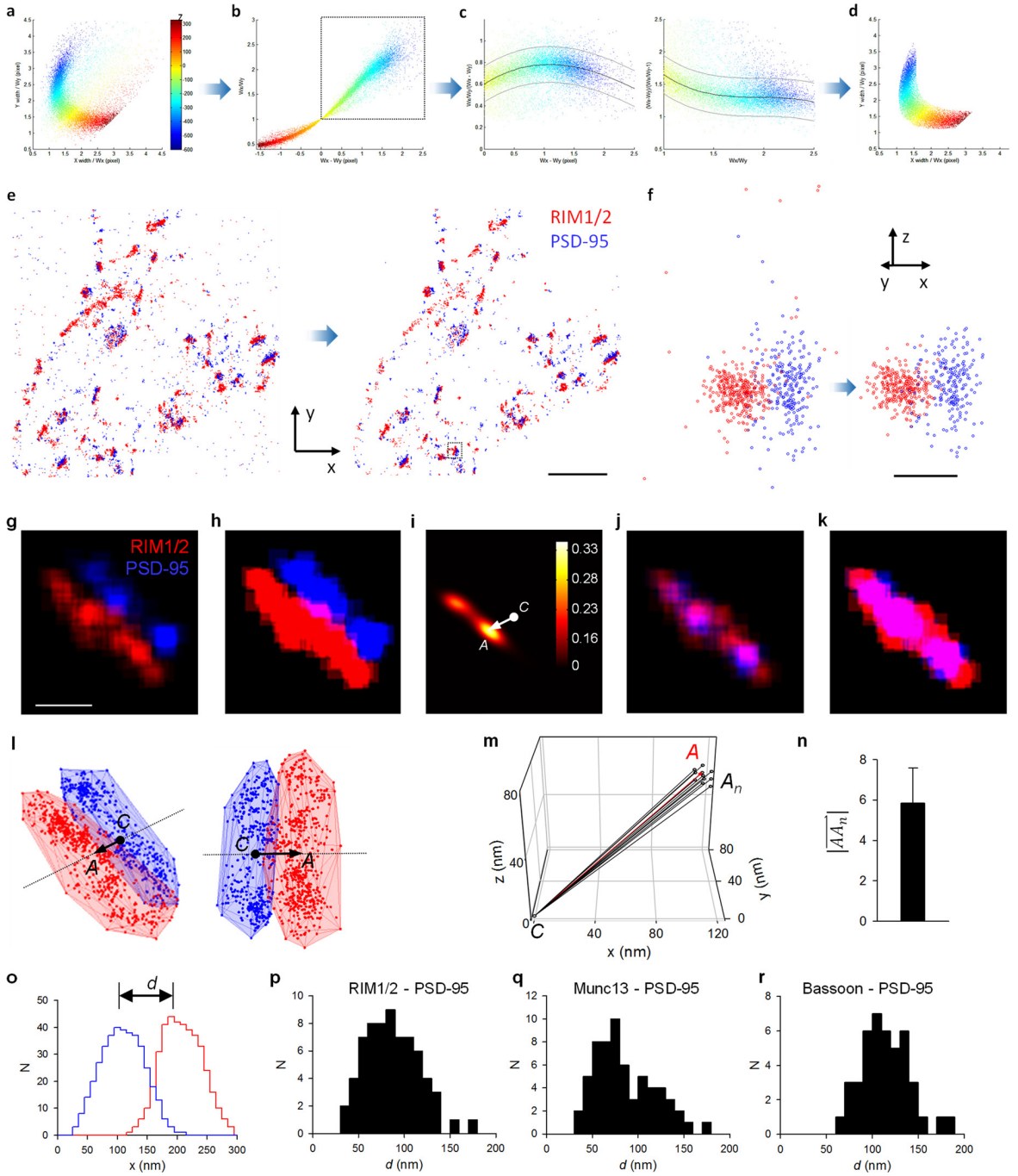

Extended Data Figure 1 | Filtering of localizations and automatic algorithm to detect the synaptic axis. **a**, Scatter plot of fitted peak width in y (W_y) against that in x (W_x). The colour codes the position in z. All localizations away from this centre dense region arise from multiple overlapping or poorly fitted peaks and should be rejected. **b**, The ellipticity (W_x/W_y) and the width difference ($W_x - W_y$) formed an approximate linear relationship when $W_x > W_y$ (dotted box). **c**, We fitted the ratios between ellipticity and the width difference to the denominators with third degree polynomial functions (black line) and rejected all localizations out of 95% confidence intervals (grey lines) of the curve (>1.96 × s.d.). The same criteria was applied to the other fraction of localizations with $W_x < W_y$. **d**, The same scatter plot as in **a** after rejection of all of the diffuse localizations (about 20–25%). **e**, **f**, The filtering protocol cleared up most of the localizations from multiple overlapping peaks or poorly fitted peaks, including most of the non-relevant background localizations (**e**) and those localizations with poorly calibrated z positions (**f**). Scale bars, 2 μm (**e**) and 200 nm (**f**). The synapse in **f** corresponds to the boxed synapse in **e**. **g**, A 2D section through the centre of the convoluted constructed 3D distribution matrix of a synapse. **h**, Peak density of the matrix set to a quarter of the mean molecule density of the synaptic cluster. **i**, 2D section at the same position of the 3D matrix of direct cross-correlation of the two channels (equation (3) in Methods). C is the centre of matrix, and A is the peak of the cross-correlation. **j**–**k**, Best overlap of the two synaptic clusters after PSD-95 was moved in 3D space along the vector $\overrightarrow{CA}$. **l**, 3D scatter plots of the synapse in two different view angles. The arrow denotes the vector and the extended line (dotted) represents the synaptic axis. **m**, 3D plot of detected synaptic axis when the positions of high-density peaks in RIM1/2 (nanoclusters) were randomized within the synaptic cluster. This simulation was performed 35 times, but only 10 representative results are presented here to avoid overlapping. The red denotes the synaptic axis of the original synaptic cluster. **n**, Averaged distance between the detected C_n positions from 35 simulated clusters to the C position of the original cluster. Data shown in mean ± s.d. This <6 nm distance confirms that the high-density peaks have negligible effect on the detection of the synaptic axis in this Method. **o**, Distribution of all localizations along the synaptic axis with bin size of 10 nm. Peak-to-peak distance between the synaptic protein pair can be measured from this distribution. **p**–**r**, Distribution of peak-to-peak distances for three pairs of synaptic proteins.

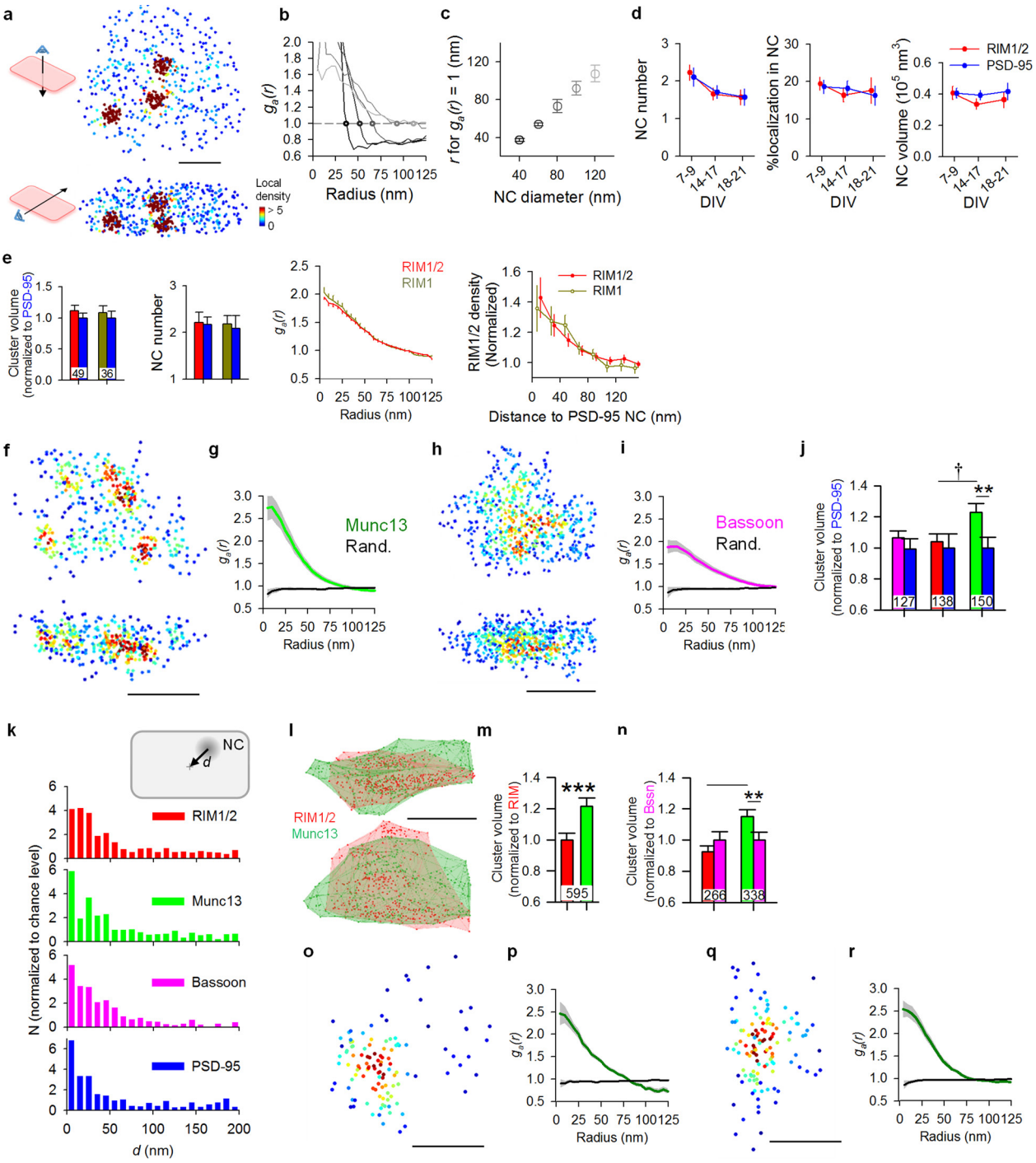

Extended Data Figure 2 | See next page for caption.

Extended Data Figure 2 | Nanocluster organization of vesicle release machinery proteins in the active zone and postsynaptic AMPA receptors. **a**, *En face* (top) and side (bottom) views of local density maps of a simulated synapse with artificial nanoclusters with 40-nm diameters. Scale bar, 100 nm. **b**, Autocorrelation function of simulated clusters with different sized nanoclusters. The points represent the radius where $g(r) = 1$. **c**, Pooled data from 15 sets of simulations showing that the radius where $g(r)$ first crosses 1 reasonably estimates the average nanocluster diameters. **d**, Comparison of nanocluster number, fraction of localization in nanocluster, and nanocluster volume across different developmental stages shows no significant difference, though the young 9 days *in vitro* (DIV) culture shows a trend towards increased nanocluster numbers (one-way ANOVA on ranks for nanocluster number and volume, one-way ANOVA for percentage localization in nanocluster). Data were from 143 RIM nanoclusters and 135 PSD nanoclusters of 64 DIV 9 synapses, 63 RIM nanoclusters and 65 PSD nanoclusters of 38 DIV 14 synapses, and 44 RIM nanoclusters and 41 PSD nanoclusters from 28 DIV 21 synapses. **e**, Comparison of two RIM antibodies (from left to right) in whole synaptic cluster volume, number of nanoclusters, autocorrelation function estimating average nanocluster diameter, and protein density relative to PSD-95 nanocluster centres. Anti-RIM1/2 (Synaptic Systems #140-203) targets the zinc-finger domain and anti-RIM1 targets the PDZ domain of RIM1 (Synaptic Systems #140-003). These tests suggest that there is no significant difference between these two antibodies. The numbers in bars denote the group sizes. **f**, Local density maps of *en face* (top) and side (bottom) views of an example Munc13 cluster. Scale bar, 200 nm. **g**, Auto-correlation functions for Munc13 distributions compared to simulated randomized distributions. **h**, **i**, Local density maps and ACF of Bsn cluster. Scale bar, 200 nm. **j**, Pooled cluster volumes, normalized to PSD-95 volumes within each synapse. Each bar pair represents data from a set of RIM1/2-PSD-95, Munc13-PSD-95 or Bsn-PSD-95 staining. The numbers in bars denote the group sizes. **k**, Distribution of *en face* distances between nanocluster centre and synapse centre. Data were normalized to the distribution of simulated clusters with the same number of nanoclusters as the original synapse but randomized positions. **l**, An example synapse with RIM1/2 and Munc13 staining of the same synapse, shown in two different angles. The translucent surfaces represent the alpha shapes that define the synaptic cluster borders. **m**, Pooled RIM1/2 and Munc13 cluster volumes, normalized to RIM1/2 within each synapse. **n**, Pooled RIM1/2, Munc13 and Bsn cluster volumes from staining of RIM1/2-Bsn and Munc13-Bsn, normalized to Bsn within each synapse. $^{*}P < 0.05$; $^{***}P < 0.001$; Wilcoxon signed-rank test. $\dagger P < 0.05$, one-way ANOVA on ranks with pairwise comparison procedures (Dunn's method). **o**, Local density map of a GluA2 cluster. **p**, Auto-correlation functions for GluA2 distributions compared to simulated randomized distributions. **q**, Local density map of a GluR2/3 cluster. **r**, Auto-correlation functions for GluR2/3 distributions compared to simulated randomized distributions. All experiments were repeated $\geq$3 times.

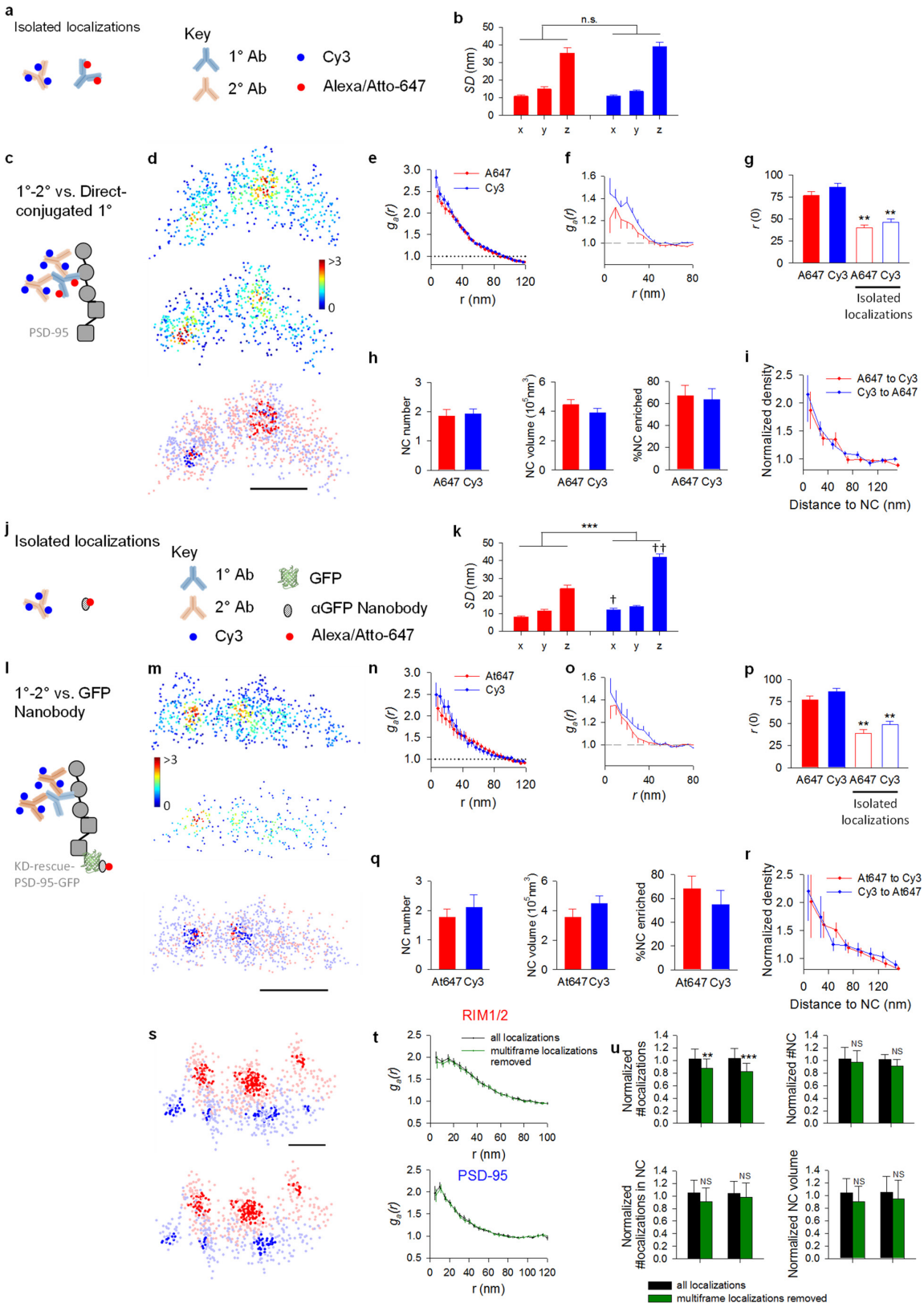

Extended Data Figure 3 | See next page for caption.

Extended Data Figure 3 | Detected nanoclusters are unlikely a result of labelling artefacts or overcounting of molecules. a–i, Comparison of PSD-95 labelled with monoclonal primary antibodies directly conjugated to Alexa647 dye (1°-A647, red) with the same molecules labelled with primary and secondary antibodies conjugated to Cy3 (1°-2°-Cy3, blue) as represented in **c**. **a**, **b**, Comparison between non-synaptic small groups of localizations arising from isolated primary antibodies and secondary antibodies. Schematic shown in **a**. Standard deviation of localizations in both groups along different dimensions ($n = 32$ for A647; $n = 36$ for Cy3) in **b**. The two types of localizations groups showed similar variation in all dimensions. **d**, Local density maps of the same PSD-95 cluster labelled with 1°-A647 (top) and 1°-2°-Cy3 (middle) and overlapped distribution of 1°-A647 and 2°-Cy3 with detected nanoclusters highlighted in darker colours (bottom). Scale bar, 200 nm. **e**, Autocorrelation of synaptic clusters labelled with 1°-A647 and 1°-2°-Cy3. **f**, Autocorrelation of isolated small groups of localizations of A647 and Cy3 dyes. **g**, Comparison of the radius at which the autocorrelation function crossed with the random level ($g(r) = 1$). There was no difference between PSD-95 clusters with different labelling methods, but the $r(0)$ for isolated localization groups were significantly less than $r(0)$ for PSD-95 clusters. $^{**}P < 0.01$, *t*-test between the filled and open bars of the same colour. **h**, Nanoclusters detected in both channels displayed no difference in number, volume, or the fraction of nanoclusters enriched with localizations from the other channel. **i**, Protein enrichment of localizations detected in each channels with those in the other channel ($n = 32$ synapses). These results demonstrate that the nanoclusters we detected in our study were not due to aggregation of multiple secondary antibodies to the primary antibodies. **j–r**, Cells transfected with knockdown-rescue-PSD-95-GFP were labelled with nanobodies against GFP conjugated at a 1:1 ratio with Atto647 (Nb-At647, red) and primary/secondary antibodies against PSD-95 (1°-2°-Cy3, blue) as depicted in **l**. **j**, **k**, Comparison between non-synaptic small groups of localizations arising from isolated Nb-At647 and 1°-2°-Cy3 (as depicted in **j**, $n = 26$ and 28, respectively). **k**, The nanobodies showed a significant smaller size than antibodies. $^{***}P < 0.001$, two-way ANOVA, $^{\dagger}P < 0.05$, $^{\dagger\dagger}P < 0.01$, pairwise comparison (Tukey test) between nanobodies and antibodies. **m–r**, Similar comparison as in **d–i** between PSD-95 clusters labelled with Nb-At647 and 1°-2°-Cy3 ($n = 13$ synapses). Scale bar, 200 nm. Overall, these results demonstrated that the nanoclusters we detected in our study were unlikely a result of artefacts of antibody binding and labelling. The difference between the size of the isolated localizations groups and PSD-95 clusters calculated by autocorrelation also argues against the possibility that the nanoclusters we detected were owing to repetitive switching of one or a few fluorophores. $^{**}P < 0.01$, *t*-test between the filled and open bars of the same colour. **s**, An example synapse with nanoclusters highlighted before (upper) and after (lower) removal of localizations resulting from fluorophores lasting for multiple frames. Scale bar, 100 nm. **t**, Paired autocorrelation function of synaptic clusters with and without multiple-frame molecules. $P = 0.77$, $n = 25$ synapses for RIM1/2; $P = 0.58$, $n = 25$ synapses for PSD-95, two-way ANOVA with repeated measures. **u**, The tracking removed $13 \pm 8\%$ and $17 \pm 9\%$ of the localizations for RIM1/2 and PSD-95, respectively, but had no significant effects on autocorrelation function results, nanocluster numbers, or nanocluster volumes. $^{**}P < 0.01$; $^{***}P < 0.001$; NS, $P > 0.05$; Wilcoxon signed-rank test. All data were pooled from ≥ 3 replicas.

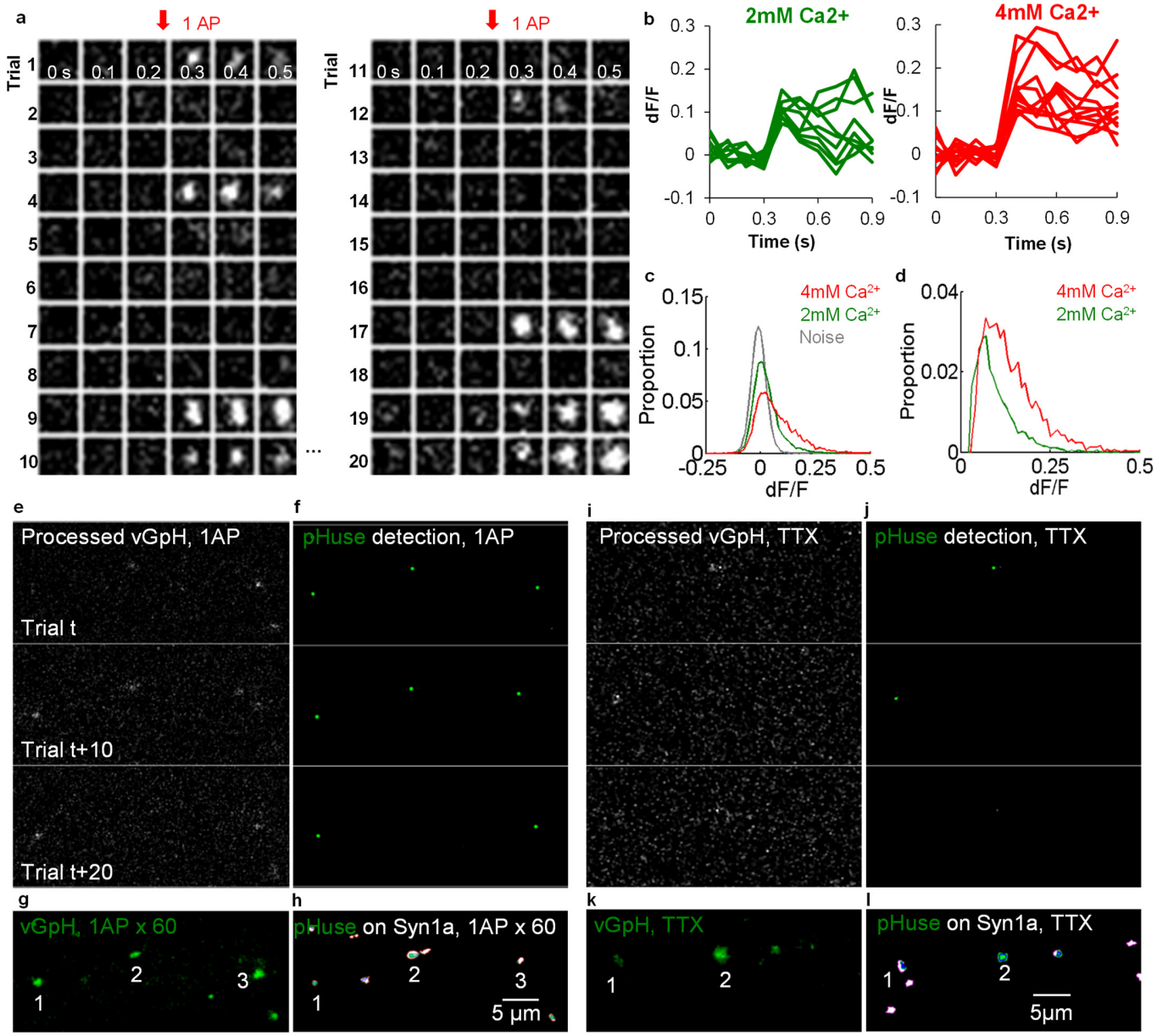

Extended Data Figure 4 | 1AP evoked release is $[Ca^{2+}]$ dependent and mainly univesicular[48]. **a**, Example of fluorescence signals at a single bouton over repeated trials of 1 action potential stimulation. **b**, Single event traces of vGpH fluorescence increase following 1 action potential stimuli in standard (2 mM) or heightened extracellular $[Ca^{2+}]$ (4 mM). **c**, Comparison of distributions of fluorescence changes in 2 mM ($n = 233/27$) and 4 mM ($n = 115/12$) extracellular $[Ca^{2+}]$, relative to noise distributions obtained from the baseline frames before stimulation. **d**, Comparison of noise-subtracted distributions of fluorescence changes in different $[Ca^{2+}]$. **e**, Processed images of vGpH fluorescence increase following 1 action potential stimuli from three trials ten trials apart. **f**, Automatic detection using pHuse of events shown in **e**. **g**, Summed projection of framewise and background subtracted vGpH fluorescence increases over 60 trials. **h**, pHuse localizations on Syn1a (white). **i–l**, Same as **e–h** for spontaneous events in TTX over 5 min. *n* given in synapses/experiments.

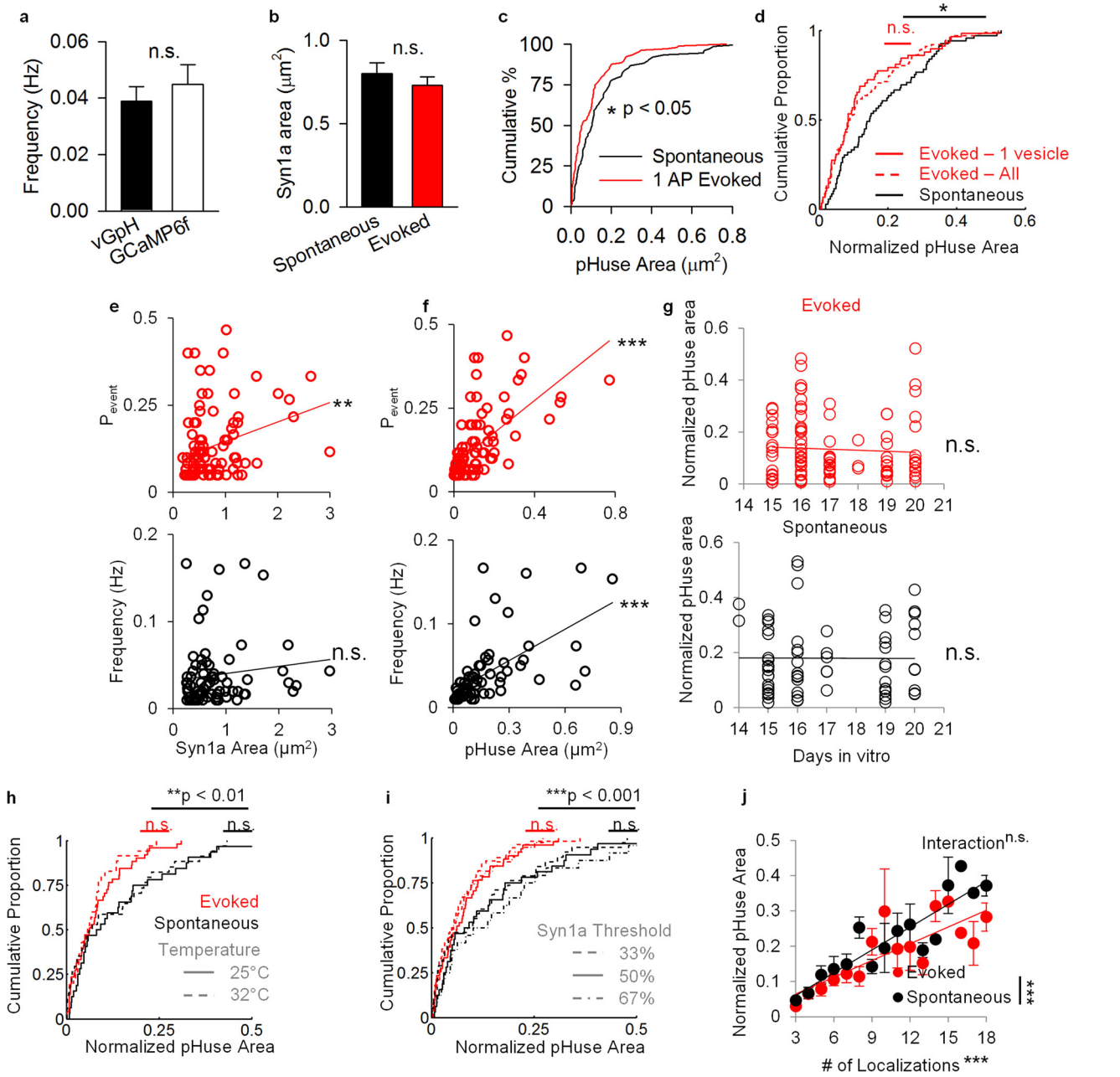

Extended Data Figure 5 | pHuse reveals differences between evoked and spontaneous fusion site areas. a, Comparison of spontaneous frequency measured presynaptically using vGpH ($n = 77/22$) and postsynaptically using GCaMP6f (ref. 45) ($n = 61/5$), $t = 1.02$, not significant. **b**, Average bouton areas across groups, $t = 0.87$, not significant. **c**, Cumulative distributions of fusion areas for spontaneous and evoked release (Kolmogorov–Smirnov test, $^*D = 0.23$) **d**, Cumulative distributions of normalized fusion areas for 1 AP evoked fusion excluding events with photon counts > mean + 2 s.d. of spontaneous events ($n = 91/27$) compared to all evoked events ($n = 104/28$, Kolmogorov–Smirnov test, $D = 0.05$, not significant) and spontaneous events ($n = 77/22$, Kolmogorov–Smirnov test, $^*D = 0.25$) **e**, **f**, Notably, while evoked P_r was significantly positively correlated with Syn1a area, as reported previously[49], spontaneous event frequency showed no relationship with Syn1a area (**e**, linear fit, evoked $^{**}R = 0.30$, spontaneous $R = 0.12$, not significant). On the other hand, both spontaneous event frequency and evoked P_r significantly positively correlated with pHuse area (**f**, linear fit, evoked $^{***}R = 0.64$, spontaneous $^{***}R = 0.60$). This suggests that pHuse area may be a better approximation for active zone area and the functional parameters of a synapse than bouton area. **g**, Normalized pHuse area as a function of cell age shows no significant correlation (evoked $R = 0.03$, not significant, spontaneous $R = 0.004$, not significant). **e**–**g**, $n_{evoked} = 104/28$, $n_{spont} = 77/22$. **h**. Normalized pHuse area was not significantly different at room temperature ($n_{evoked} = 51/10$, $n_{spont} = 32/7$) versus physiological temperature ($n_{evoked} = 35/9$, $n_{spont} = 34/4$) within modes of release but still significantly different between modes of release. **i**, Normalized pHuse area was not significantly different at different thresholds for Syn1a within modes of release but still significantly different between modes of release ($n = 51/10$). **j**, Both numbers of events and mode of release are significant factors for pHuse area, but they do not have a significant interaction $n_{evoked} = 155/38$, $n_{spont} = 109/29$. For **i**, **j**, see Supplementary Tables for statistics. n given in synapses/experiments, $^*P < 0.05$; $^{**}P < 0.01$; $^{***}P < 0.001$.

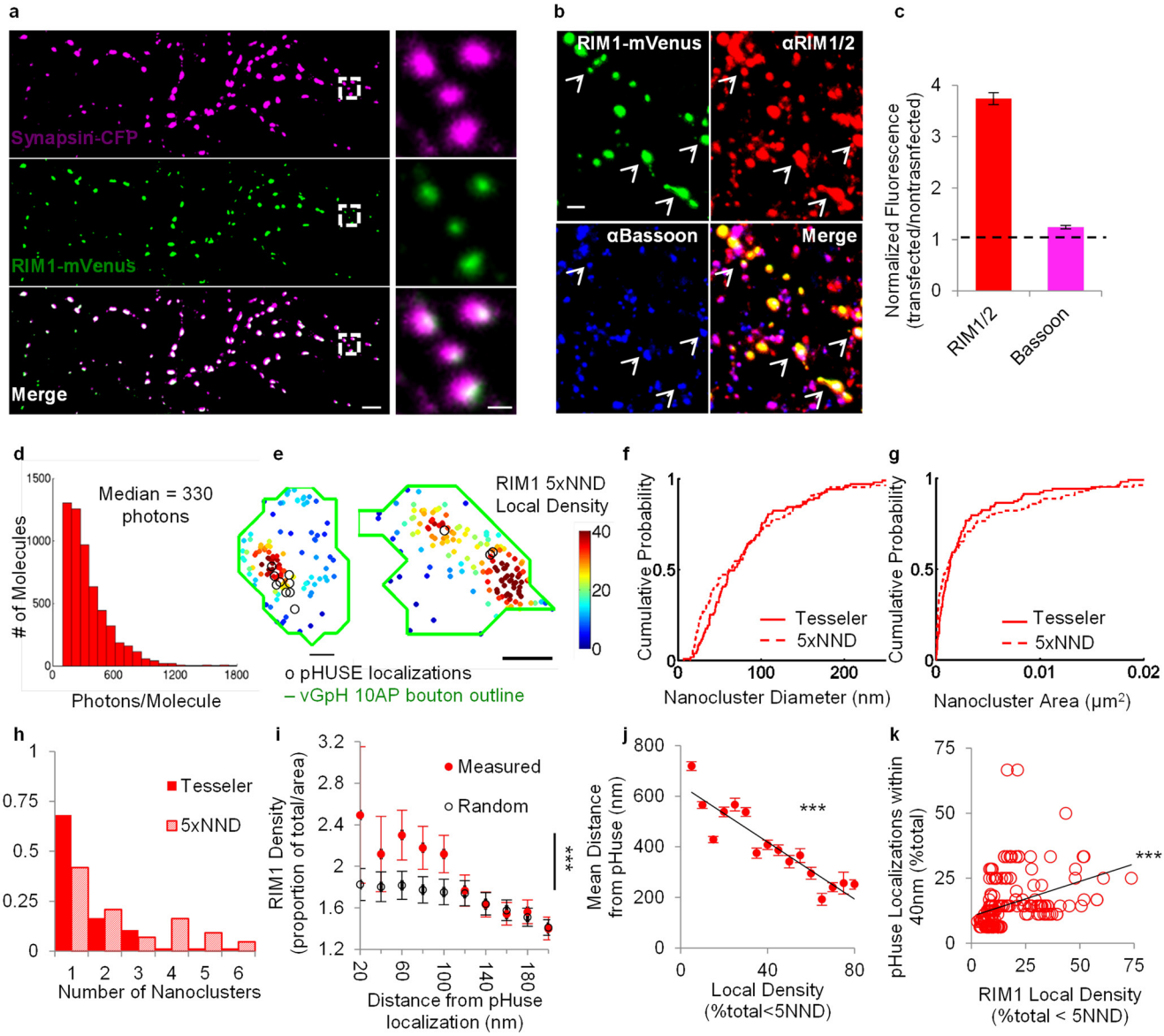

Extended Data Figure 6 | RIM1-mEos3.1 PALM identifies nanoclusters. **a**, Neurons co-expressing RIM1-mVenus (a gift from P. Kaesar) and Syn1a–CFP colocalize to the same boutons. Right panels show enlargement of areas within the white boxes. Scale bars, 5 μm (left) and 1 μm (right). **b**. Neurons expressing RIM1-mVenus immunostained for RIM1/2 and Bsn. Arrowheads point to some colocalized active zones. Scale bar, 2 μm. **c**, Immunofluorescence intensity of transfected cells normalized to nearby untransfected cells show 3.74 ± 0.11-fold overexpression of RIM and 1.24 ± 0.03-fold increase in Bsn ($n = 262$ synapses/7 cells). **d**, Photon count distribution of RIM1-mEos3.1 (3997 localizations). **e**, Same boutons shown in Fig. 2 visualized using 5 × nearest neighbour density (NND) as a measure of local density. **f**–**h**, Cumulative distributions of PALMed RIM1 nanoclusters diameter, area, and number, respectfully, identified using adapted Tesseler analysis and 5 × NND analysis ($n = 65/13$). **i**, RIM1 localization density as a function of radial distance from pHuse localizations. (See Supplementary Tables for statistics.) **j**, Mean distance from pHuse localizations as a function of local density measured by 5 × NND (raw data ***$R = 0.23$, $n = 26/13$). **k**, Proportion of pHuse localizations within 40 nm of a RIM1 localization as a function of RIM1 local density measured by 5 × NND (***$R = 0.35$). *n* given in synapses/experiments unless otherwise specified, ***$P < 0.001$.

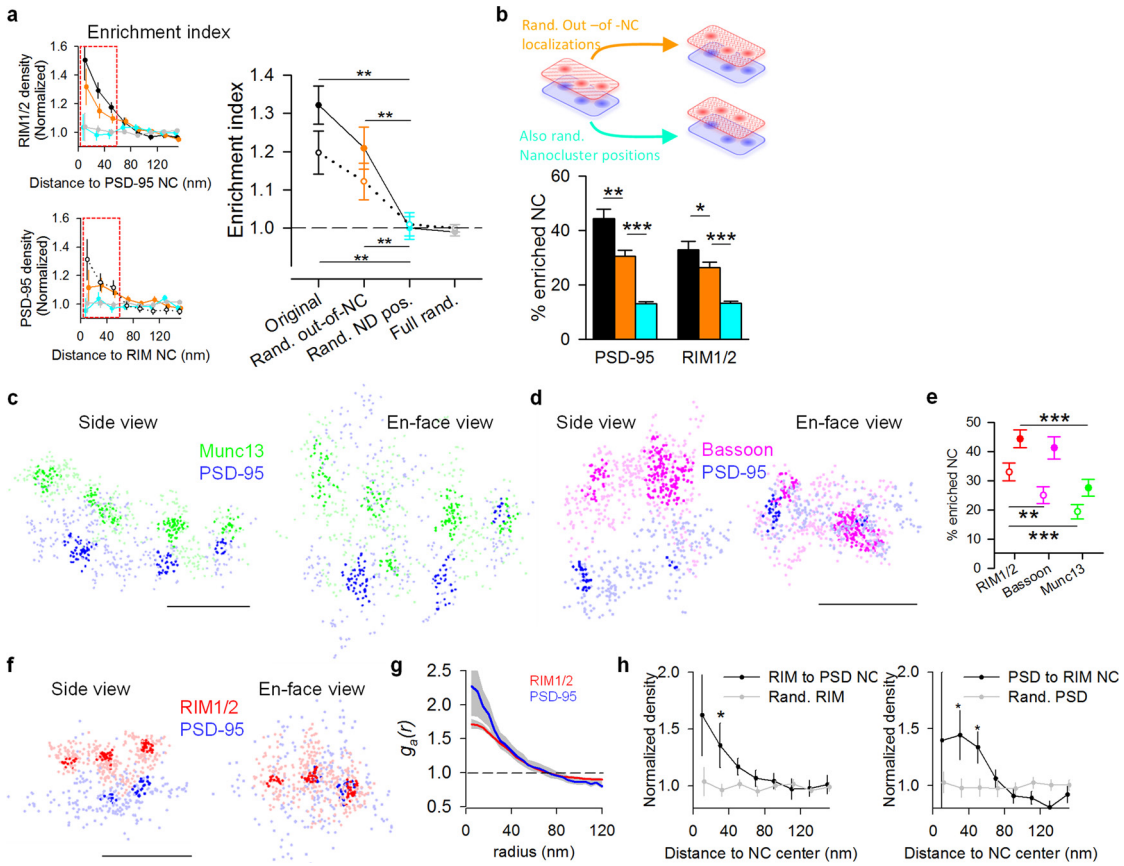

Extended Data Figure 7 | Protein enrichment within nanocolumns. **a**, Enrichment index between RIM1/2 and PSD-95. The left insets are replicas of Fig. 3e, and the enrichment index is defined as the average of the first three bins in the enrichment profile (boxed), that is, normalized localization density within 60 nm from the projection centre of a given nanocluster. Filled points show RIM1/2 relative to PSD-95 nanoclusters, open points show PSD-95 relative to RIM1/2 nanoclusters. Same randomizations as in Fig. 3e and depicted again in **b**. $^{**}P < 0.01$; $^{***}P < 0.001$, one-way ANOVA on ranks with pairwise comparison procedures (Dunn's method). **b**, The fraction of enriched nanoclusters is significantly above chance level, and is also dependent on the relative position of the two sets of nanoclusters. **c**, **d**, Side and *en face* views of a synaptic Munc13 and PSD-95 pair and a synaptic Bsn and PSD-95 pair with highlighted nanoclusters. Scale bar, 200 nm. **e**, Pooled enrichment index of three active zone proteins and PSD-95. Scale bar, 200 nm. Filled points show active zone proteins relative to PSD-95 nanoclusters, open points show PSD-95 relative to active zone protein nanoclusters. $^{**}P < 0.01$; $^{***}P < 0.001$, one-way ANOVA on ranks with pairwise comparison procedures (Dunn's method). **f**, Example of RIM1/2 and PSD-95 in adult hippocampal slices. **g**, Auto-correlation functions of RIM1/2 and PSD-95 ($n = 192$ and 43 synapses, respectively). There were, on average, 2.02 ± 0.08 and 1.32 ± 0.21 nanoclusters with a volume of (3.6 ± 0.2) and $(4.2 \pm 0.7) \times 10^5$ nm^3 for RIM1/2 and PSD-95, respectively. Except PSD nanocluster number which was significantly less than that in cultures ($P = 0.03$), all other parameters were similar (Wilcoxon signed-rank test). **h**, Enrichment profile between RIM1/2 and PSD-95 in tissue slices (28 synapses from 7 sections, 4 animals). $^{*}P < 0.05$ between measured and randomized synapses, two way ANOVA with pairwise comparison procedures (Dunn's method).

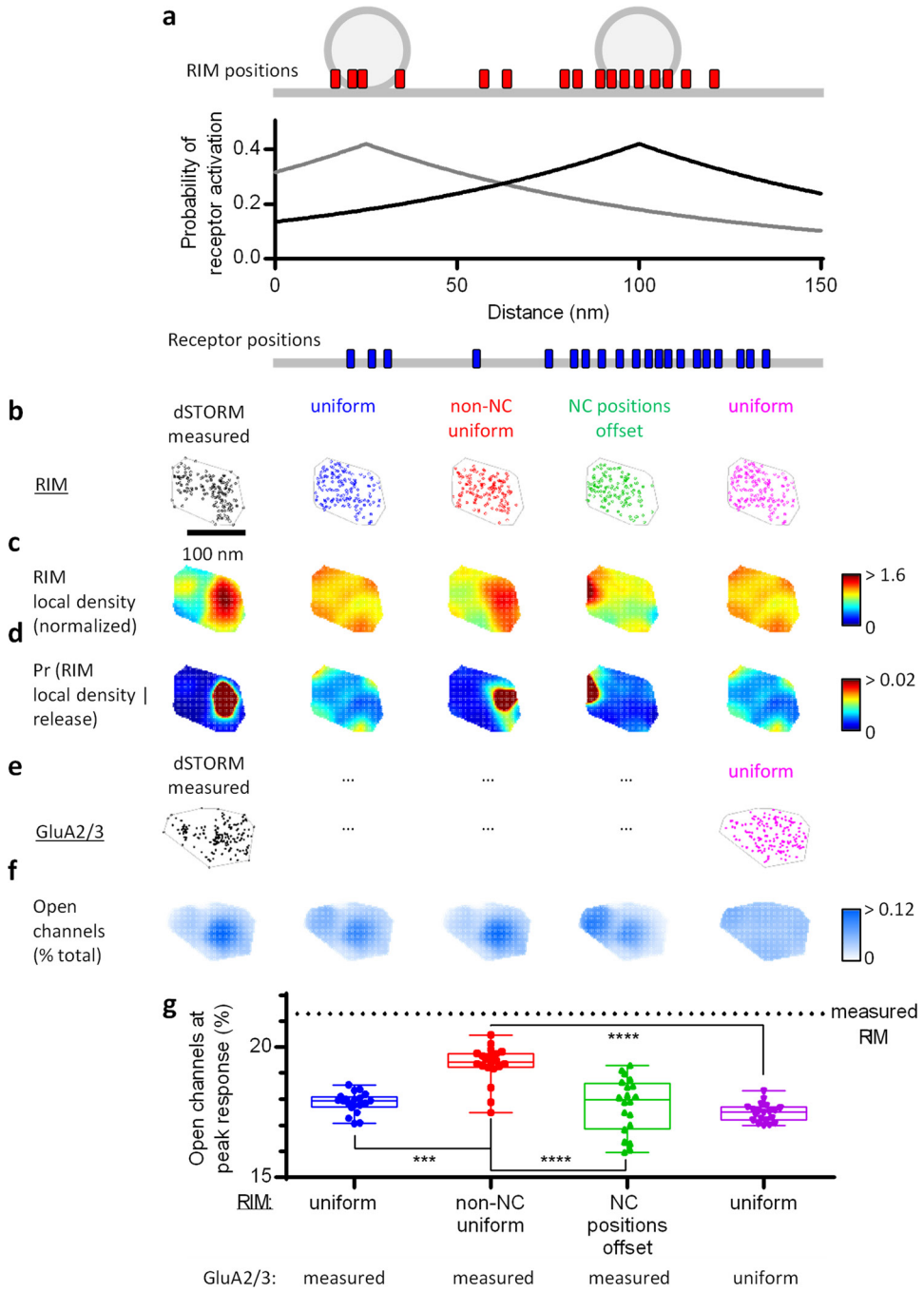

Extended Data Figure 8 | Preferential release in nanocolumns can increase synaptic strength. a, Schematic of the experimentally constrained, deterministic approach used to study the dependence of synaptic strength on the spatial distribution of release sites and AMPARs. The simulated release site distribution at a synapse was drawn from its measured RIM positions and the average measured relationship between RIM density and pHuse locations (Fig. 2). **b**, Distributions of measured RIM localizations within a single active zone (active zone) boundary (grey), and the same cluster with randomized positions of the indicated subsets of molecules. **c**, Maps of RIM local density normalized to the overall densities within the active zones. **d**, Probability density maps of possible release sites given that a release occurs. **e**, Distributions of GluA2/3 locations within the PSD boundary (grey) of the same measured synapse (ellipses refer to this distribution) and randomized. **f**, Maps of fraction of open channels at peak response per average release from the respective active zones directly above them in **d**. **g**, Calculated open channels at peak response, $n = 20$ randomly generated molecular distributions. See Methods for more details.

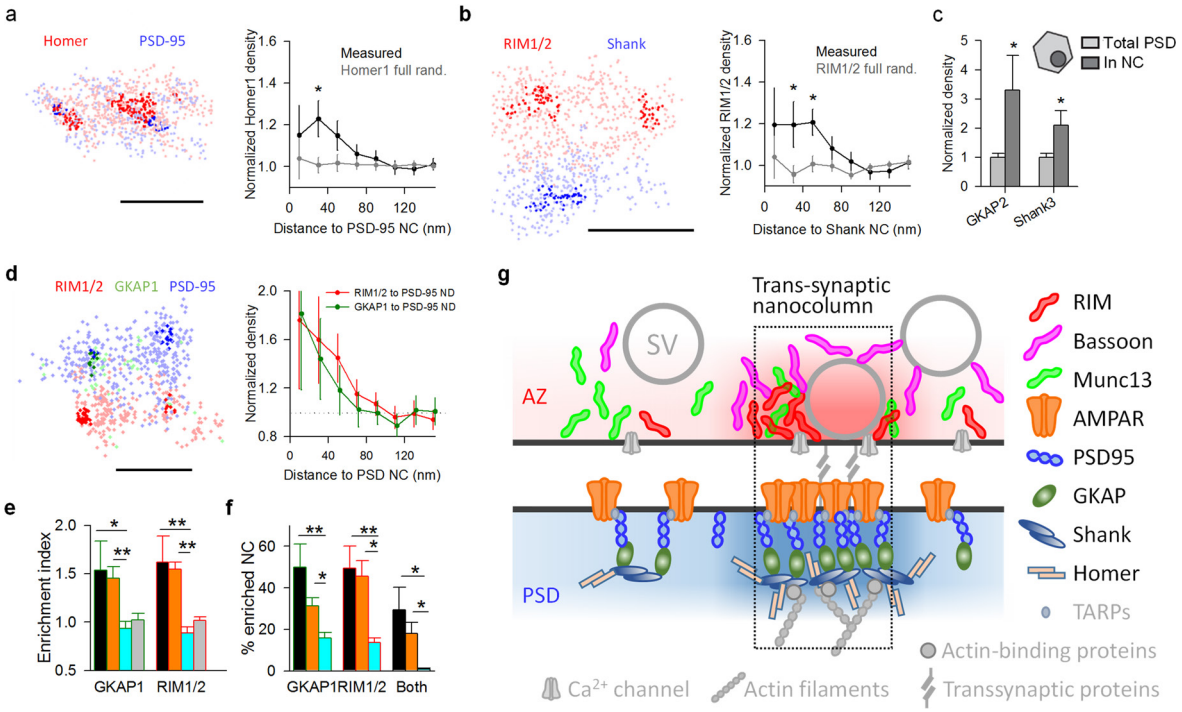

Extended Data Figure 9 | Enrichment of other scaffolding proteins within nanocolumns. a, Enrichment of Homer1 with PSD-95 nanoclusters, $n = 118$ nanoclusters from 48 synapses, scale 100 nm. **b**, Enrichment of RIM1/2 to Shank nanoclusters, $n = 80$ nanoclusters from 32 synapses. Scale bar, 200 nm. $^*P < 0.05$, ANOVA on ranks with pairwise comparison procedures (Dunn's method) in **a** and **b**. **c**, GKAP2 and Shank3 densities (determined with STORM, $n = 6$ and 12, respectively) within PSD-95 nanoclusters (determined with PALM of transfected knockdown-replacement-PSD-95-mEos2) normalized to total PSD densities. Both proteins showed significant enrichment in PSD-95 nanoclusters, $^*P < 0.05$, paired t-tests. **d**, Three-colour STORM imaging of RIM1/2, GKAP1 and PSD-95 on the same synapses example (left) and protein enrichment profiles of RIM1/2 and GKAP1 with respect to PSD-95 nanoclusters (right), $n = 32$ nanoclusters from 17 synapses. Scale bar, 200 nm. **e**, Enrichment indices of RIM1/2 and GKAP1 relative to PSD-95 nanoclusters. Colour-coded bars represent the same set of randomizations as performed in Fig. 3c: orange denotes randomization of only out-of-nanocluster localizations, cyan denotes randomization of nanocluster positions within synaptic clusters and grey denotes randomization of all localizations. **f**, The percentage of PSD-95 nanoclusters that were enriched with GKAP1, RIM1/2 or both with colour-coded randomizations. $^*P < 0.05$; $^{**}P < 0.01$, ANOVA on ranks with pairwise comparison procedures (Dunn's method), $n = 32$ nanoclusters from 17 synapses in 7 different cultures. **g**, Schematic summary of the distribution of synaptic proteins within nanocolumns. The distributions of colour-coded proteins are based on our results and the proteins in grey are hypothetical, some, such as Ca^{2+} channels, have been suggested previously to be clustered[49,50]. All experiments were repeated ≥ 5 times.

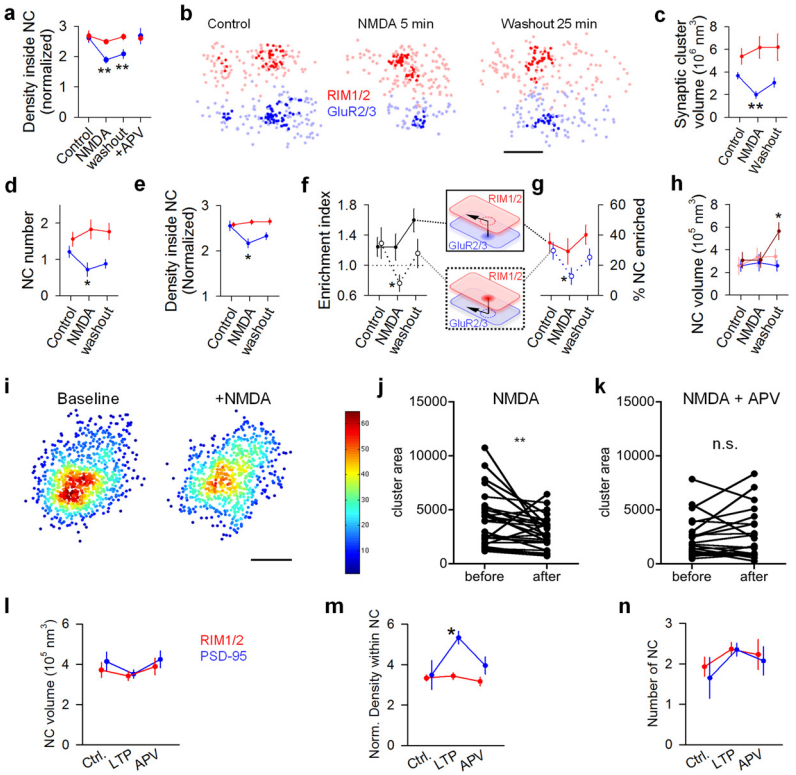

Extended Data Figure 10 | Plasticity within nanocolumns. a, Changes in the localization density within RIM1/2 (red) and PSD-95 (blue) nanoclusters under control, 5 min NMDA treatment, 25 min washout, and NMDA + AP5 treatment conditions. **b**–**h**, Reorganization of RIM1/2 and GluR2/3 under control, 5 min NMDA treatment, 25 min washout conditions examples (**b**), comparison of whole synaptic cluster sizes (**c**), nanocluster number per synapse (**d**), localization density within nanoclusters (**e**), enrichment indices (**f**), percentage of nanoclusters that were enriched (**g**), and nanocluster volumes (**h**). Note that similar to the results from the RIM1/2-PSD-95 analyses, only those RIM1/2 nanoclusters that were enriched with GluR2/3 (dark red) were increased in volume. $^{*}P < 0.05$; $^{**}P < 0.01$, ANOVA on ranks with pairwise comparison to control group (Dunn's method), and χ^2 test for the proportion. Data from 62, 21 and 37 nanoclusters from 34, 18 and 24 synapses for control, NMDA, and washout, respectively. **i**, Colour-coded local density map of an example live-PALMed PSD-95 cluster before and after NMDA treatment. Scale bar, 100 nm. **j**, **k**, Changes in PSD-95 nanocluster area induced by NMDA and blocked by AP5 ($n = 28$ and 21, respectively). $^{**}P < 0.01$, NS, not significant, paired t-test. **l**–**n**, LTP stimulation induced changes in nanocluster volumes (**l**), localization density within nanoclusters (**m**) and nanocluster numbers (**n**). $^{*}P < 0.05$, ANOVA on ranks with pairwise comparison to control group (Dunn's method). All experiments were repeated $\geq$5 times.